

# Analysing stress field conditions of the Colima Volcanic Complex (Mexico) by integrating FEM simulations and geological data

Silvia Massaro<sup>1,2</sup>, Roberto Sulpizio<sup>1,2,3</sup>, Gianluca Norini<sup>2</sup>, Gianluca Groppelli<sup>2</sup>, Antonio Costa<sup>1</sup>, Lucia Capra<sup>4</sup>, Giacomo Lo Zupone<sup>5</sup>, Michele Porfido<sup>6</sup>, Andrea Gabrieli<sup>7</sup>

<sup>1</sup>Istituto Nazionale di Geofisica e Vulcanologia, Via D. Creti 12, 40128, Bologna, Italy

<sup>2</sup>Istituto di Geologia Ambientale e Geoingegneria, Consiglio Nazionale delle Ricerche, Via M. Bianco 9, 20131, Milan, Italy

<sup>3</sup>Dipartimento di Scienze della Terra e Geoambientali, Via E. Orabona 4, 70125, Bari, Italy

<sup>4</sup>Centro de Geociencias, Universidad Nacional Autonoma de Mexico, Queretaro, Mexico

<sup>5</sup>Institute of New Energy and Low-carbon Technology, Sichuan University, Chengdu, PRC

<sup>6</sup>Alumni Mathematica, Dipartimento di Matematica, Via E. Orabona 4, 70125, Bari, Italy

<sup>7</sup>Hawai'i Institute of Geophysics and Planetology, 1680 E-W Road, Honolulu, Hawai'i 96922, USA

\*Corresponding author: Silvia Massaro ([silvia.massaro@ingv.it](mailto:silvia.massaro@ingv.it)).

## Abstract

In recent decades, Finite Element Modelling (FEM) has become a very popular tool in volcanological studies, and has been used to describe even complex system geometries, accounting for multiple reservoirs, topography and heterogeneous distribution of host rock mechanical properties. In spite of this, the influence of geological information on numerical simulations is still poorly considered. In this work, a 2D Finite Element Modelling FEM of the Colima Volcanic Complex (Mexico) is provided by using the LInear Static Analysis (LISA) software, in order to investigate the stress field conditions at increasing detail of geological data. By integrating the published geophysical, volcanological and petrological data, we modelled the stress field considering either one or two magma chambers connected to the surface via dykes or isolated (not connected) in the elastic host rocks (considered homogeneous and non homogeneous). We also introduced tectonic disturbance, considering the effects of direct faults bordering the Colima Rift and imposing an extensional far- field stress of 5 MPa. We ran the model using gravity in the calculations. Our results suggest that an appropriate set of geological data is of pivotal importance for obtaining reliable numerical outputs, which can be considered as a proxy for natural systems. Beside and beyond the importance of geological data in FEM simulations, the model runs using the complex feeding system geometry and tectonics show how the present-day Colima volcanic system can be considered in equilibrium from any stress state point of view, in agreement with the long- lasting open conduit dynamics that have lasted since 1913.

## 37 **1 Introduction**

38

39 Magmatism and tectonism are strongly related to regional and local stress fields, affecting both the  
40 orientation of faults and the location of volcanic vents (Geyer et al., 2016). The stress field around a  
41 magmatic source originates from three main contributions: (1) the background stress, composed of a  
42 vertical gravitational load, a lateral horizontal load (lithostatic confinement) and tectonic regime;  
43 (2) the stress field caused by the loading of the volcano edifice; and, (3) the stress field generated by  
44 the magmatic pressure (e.g. Martí and Geyer, 2009; Currenti and Williams et al., 2014). In recent years,  
45 a large number of semi-analytical and numerical methods have been proposed for the solution of the  
46 stress field state of natural systems (e.g. Cayol and Cornet, 1998; Simms and Garven, 2004; Manconi  
47 et al., 2007; Long and Grosfils, 2009; Currenti et al., 2010; Currenti and Williams et al., 2014; Zehner  
48 et al., 2015), taking into account the static elastic deformation in a multi-layered half-space (e.g.  
49 Dieterich and Decker, 1975; Bonafede et al., 2002; Wang et al., 2003; Gudmundsson and Brenner,  
50 2004; Pritchard and Simons, 2004; Zhao et al., 2004; Pritchard and Simons, 2004; Gottsmann et al.,  
51 2006; Geyer and Gottsmann, 2010; Zhong et al., 2019). Following the successful application in  
52 mechanical engineering, fluid dynamics and thermodynamics (e.g., Gutiérrez and Parada, 2010;  
53 Gelman et al., 2013), the use of Finite Element Modelling method (FEM) has been introduced extensively  
54 introduced in volcanology, in order to investigate the effects of topography, lithologic heterogeneities,  
55 tectonic stresses and the gravity field on the stress state of volcanic systems (e.g. Fujita et al., 2013;  
56 Bunney, 2014; Carcho and Galán del Sastre, 2014; Hickey et al., 2015; Bunney, 2014; Ronchin et al.,  
57 2015; Hickey et al., 2015; Cabaniss et al., 2019; Rivalta et al., 2019).

58 There are several examples of the use of FEM for volcanic systems has several examples, which  
59 spanning from the influence of layered materials on the surface deformation process during volcanic  
60 inflation (e.g. Darwin volcano, Galapagos Islands; Manconi et al., 2007; Albino et al., 2010) to  
61 processes affecting chamber rupture (e.g. Grosfils, 2007; Long and Grosfils, 2009).

62 The local stress around a volcanic feeding system depends on the geometry of the magma plumbing  
63 system, including the chamber(s) and dykes forming it, and on the mechanical properties of the host  
64 rock around it (e.g. Martí and Geyer, 2009), and especially on changes in Young modulus (e.g.  
65 Gudmundsson et al., 2011; Jeanne et al., 2017; Heap et al., 2020). For instance, limestone, lava flows,  
66 welded pyroclastic deposits and subvolcanic rocks can be very stiff (high Young modulus; ca. 1.7–  
67 27 GPa for limestones, Touloukian, 1981; ca. 5.4 GPa for volcanic rocks, Heap et al., 2020), but young  
68 and non-welded pyroclastic units may be very soft (low Young modulus; ca. 1.7 – 3.1 GPa, Margottini  
69 et al., 2013). Therefore, the local stress may change abruptly change from one layer to another (e.g.,  
70 Gudmundsson, 2006). Irrespective of the scope of the numerical investigation, the importance of  
71 applying accurate physical constraints to FEM hwas already been discussed in many studies (e.g., Folch  
72 et al., 2000; Fernandez et al., 2001; Newman et al., 2001; Fernandez et al., 2001; Currenti et al., 2010;  
73 Geshi et al., 2012). However, in the last decade, few investigations have been carried out to assess the  
74 influence of the amount and quality of geological data ointo FEM computations (Kinvig et al., 2009;  
75 Norini et al., 2010, 2019; Cianetti et al., 2012; Ronchin et al., 2013; Chaput et al., 2014; Norini et al.,  
76 2019). To bridge this gap, in this work we used the LInear Static Analysis (LISA) software (version  
77 8.0; [www.lisafea.com](http://www.lisafea.com)) to study the subsurface stress field state inat the Colima Volcanic Complex  
78 (CVC, Mexico) at increasing geological detail.

79 The CVC area is a good candidate for testing the response of FEM software against different geological  
80 conditions, being constituted by a large volcanic complex (Lungarini et al., 2005) within a tectonic  
81 graben filled with volcanoclastic material (Fig. 1a; Norini et al., 2010, 2019). The FEM was run starting  
82 from simple homogeneous vs stratified lithology of the subsurface, and in successively more detail by  
83 the addition of single and double magma chambers, feeder dykes, faults and extensional far-field  
84 tectonic stress (Fig. 1b).

85

86

## 87 **2 The Colima Volcanic Complex (Mexico)**

88

### 89 *2.1 Geological framework*

90 The Pleistocene–Holocene CVC is one of the most prominent volcanic edifices within the Trans-  
91 Mexican Volcanic Belt (TMVB) (Macías et al., 2006; Capra et al., 2016; Norini et al., 2019; Fig. 1a).  
92 In this area, the Rivera microplate and the Cocos plate subduct beneath the North America plate along  
93 the Middle American Trench (Stock and Lee, 1994), forming a triple junction that delimits the tectonic  
94 units known as the Jalisco Block (JB) and the Michoacán Block (MB) (Luhr et al., 1985; Allan, 1986;  
95 Rosas-Elguera et al., 1996, 1997; Ferrari and Rosas-Elguera, 1999; Rosas-Elguera et al., 2003; Frey et  
96 al., 2007). The three rifts of this system are the Tepic–Zacoalco Rift (TZR), Chapala–Tula Rift (CTR)  
97 and Colima Rift (CR). The still-active NS-trending CR was formed during a rifting phase which  
98 occurred after the Late Cretaceous–Paleogene compressive and transpressive phase (Allan, 1986; Serpa  
99 et al., 1992; Bandy et al., 1995; Cortés et al., 2010). While opening, the CR was gradually filled with  
100 Pliocene–Quaternary lacustrine sediments, alluvium and colluvium (e.g. Allan, 1986; Allan et al.,  
101 1991; Norini et al., 2010). The geometry, kinematics and dynamics of the CR have been studied on the  
102 basis of field, seismic and geodetic data, mainly collected in its northern and central sectors (see Fig. 1  
103 in Norini et al., 2010).

104 The magnitude of vertical displacement of the northern and central sectors is ca. 2.5 km by adding the  
105 topographic relief of the bounding fault scarps (1.5–1.6 km) to the calculated sediment depth (Allan,  
106 1985; Serpa et al., 1992). Field data and focal mechanism solutions are consistent with a direction of  
107 opening of the northern and central sectors oriented from E–W to NW–SE, with mainly normal and  
108 minor right-lateral displacements of the bounding faults (Barrier et al., 1990; Suárez et al., 1994; Rosas-  
109 Elguera et al., 1996; Garduño-Monroy et al., 1998; Norini et al., 2010, 2019). In contrast to field and  
110 seismic evidence of long-term slightly dextral oblique extension, recent GPS geodetic measurements  
111 suggest a possible left oblique extension of the CR (Selvans et al., 2011). In both cases, the stress

112 regime is extensional with an E–W orientation of the minimum horizontal stress in the CVC basement  
113 (Barrier et al., 1990; Suárez et al., 1994; Rosas-Elguera et al., 1996; Norini et al., 2010; Selvans et al.,  
114 2011; Norini et al., 2019).

115 The CVC stands within the central sector of the CR, on top of Cretaceous limestone, Late Miocene–  
116 Pleistocene volcanic rocks and Pliocene–Holocene lacustrine sediments, alluvium and colluvium  
117 (Allan, 1985, 1986, 1991; Cortés, 2005; Norini et al., 2010; Escudero and Bandy, 2017). It is formed  
118 by three andesitic stratovolcanoes: Cantaro (2900 m a.s.l.), Nevado de Colima (4255 m a.s.l.) and, in  
119 the southern part, the youngest and active Volcàn de Colima (3763 m a.s.l.) (Norini et al., 2019 and  
120 reference therein; Fig. 1a).

121

## 122 *2.2 Eruptive activity*

123 The eruptive history of the CVC started in the northeast area with the formation of Cantaro volcano at  
124 ca. 1–1.5 Ma followed by Nevado de Colima at ca. 0.53 Ma, which is composed of voluminous  
125 andesitic lava domes and deposits associated with caldera-forming eruptions and partial sector  
126 collapses (Robin et al., 1987; Roverato et al., 2011; Roverato and Capra, 2013; Cortés et al., 2019).

127 The youngest – Volcàn de Colima – comprises the Paleofuego edifice, which suffered several sector  
128 collapses that formed a horseshoe-shaped depression where the new active cone (also known as Volcàn  
129 de Fuego) grew up. Its activity was characterized by dome growths and collapses, extrusion of lava  
130 flows, and Vulcanian and occasionally sub-Plinian explosive eruptions (Saucedo et al., 2010; Massaro  
131 et al., 2018, 2019).

132

## 133 *2.3 The CVC plumbing system*

134 Seismic tomography (Spica et al., 2017) highlights a 15 km-deep low velocity body (LVB), which was  
135 interpreted as a deep magma reservoir. It is confined within the CR, suggesting a structural control of  
136 the normal fault system on it (Spica et al., 2014). The LVB has an extent of ca. 55 km × × 30 km in

137 the N–S and E–W directions, respectively, showing an averaged thickness < 8 km. Escudero and  
138 Bandy (2017) obtained a higher- resolution tomographic image of the CVC subsurface area, showing  
139 that the most active magma generation zone is now under the Fuego de Colima edifice. The ambient  
140 seismic noise tomographic study of Spica et al. (2014) indicates a shallow magma chamber above ca.  
141 7 km depth, in agreement with petrological studies (Medina-Martinez et al., 1996; Luhr, 2002; Zobin  
142 et al., 2002; López-Loera et al., 2011; Reubi et al., 2013, 2019; Macíasias et al., 2017; Reubi et al.,  
143 2019). Cabrera-Gutiérrez and Espíndola (2010) suggested the shallow active magma storage has a  
144 volume of ca. . 30 30 km<sup>3</sup>. It is connected to the surface by conduits, whose path is facilitated by the  
145 presence of the CR fault zone, which provide a natural pathway for fluids (e.g., Allan, 1986; Norini et  
146 al., 2010, 2019). The arrangement of dykes and the alignment of the volcanic centres of the CVC  
147 suggest that the dykes swarms draining the magma chambers developed along the NNE–SSW-  
148 trending, steep, eastward- dipping normal fault exposed on the northern CVC flank (Norini et al., 2010,  
149 2019).

150 Massaro et al. (2018) provided a first-order geometrical reconstruction of the Fuego de Colima feeding  
151 system during the 1913 sub-Plinian eruption, using volcanological data (Saucedo et al., 2010; Bonasia  
152 et al., 2011; Saucedo et al., 2011) as inputs and constraints for numerical simulations. Results showed  
153 good matches for a hybrid configuration of the shallow conduit feeding system composed of a ca. 5500  
154 5500 m- long, 200–2000 m- wide, and 40 m width dyke passing into a shallower (500 m long, 40 m  
155 diameter) cylindrical conduit. The shallow magma chamber top was set at 6 km of depth, and dyke–  
156 cylinder transition at 500 m below the summit as inferred from geophysical data (Salzer et al., 2014;  
157 Aràmbula et al., 2018).

158

159

## 160 **3 Methods**

161

162 In this study, we used the commercial 8.0 version of LISA ([www.lisafea.com](http://www.lisafea.com)), a general-purpose Finite  
163 Element Analysis (FEA) software program developed in the 1990s and based on the formulations  
164 proposed by Rao (1989), and successively integrated from other sources (Bathe, 1990; Michaeli, 1991;  
165 Schwarz, 1991; Babuska et al., 1995). Despite LISA originally being used for structural analysis (Rao,  
166 1989, 2013), it successfully predicts the stress–strain behaviour of rock masses in elastic models, in  
167 particular the deformation mechanisms even in layered rock masses (Gabrieli et al., 2015).

168

### 169 *3.1 Modelling approach*

170 The stress field of the CVC plumbing system is simulated considering an E–W cross-section, parallel  
171 to the extension associated with the active CR (Norini et al., 2010, 2019) as shown in Figure 1a–b (a–  
172 a’).

173 Since the extent of the CVC magma chambers in the NNE–SSW direction is typically much longer  
174 than the dimensions of the E–W cross-section (Spica et al., 2017), 2D solutions of either numerical or  
175 analytical models describing E–W elongated magma chambers in the crust can be reasonably adopted  
176 (Jaeger et al., 2009; Costa et al., 2011). A topographic profile and 2D plane along the chosen E–W  
177 cross-section of the CVC area was obtained in ESRI ArcGIS from a Digital Elevation Model (DEM,  
178 resolution 50 m; Instituto Nacional de Estadística y Geografía – INEGI <https://en.www.inegi.org.mx/>)  
179 and imported into Autodesk Auto-Cad R13 using a third-degree spline approximation. The IGES file  
180 was then imported into LISA for the mesh discretization.

181 The investigated domain extends  $60 \times 30$  km in an  $x$ – $z$  Cartesian Coordinate System with three- and  
182 four-node finite element discretization (Table 1). Zero normal displacements are assigned at the bottom  
183 and the lateral boundaries, while the upper boundary represents the free-stress ground surface (Fig. 1c).

184 The FEM is carried out using a plane strain approximation, implying that the deformation in the third  
185 direction is assumed to be negligible.

186 As reported by Zehner et al. (2015), FEM of geological structures requires accurate discretization of  
187 the computational domain. It follows that the unstructured tetrahedral meshes have to fulfil the  
188 following requirements: i) sufficient mesh quality: the tetrahedrons should not be too acute-angled,  
189 since numerical instabilities can occur; ii) incorporation of geometry for defining boundary conditions  
190 and constraints; and iii) local adaption, which is a refinement of the mesh in the vicinity of physical  
191 sources in order to avoid numerical errors during the simulation. In this work, we adopted a mesh  
192 composed of 4660 plane continuum elements, which have been refined in the regions of higher  
193 gradients (i.e. near the contours of the magmatic feeding system).

194 In our simulations, the extent of the rock layers (Table 2) refers to that used by Norini et al. (2010,  
195 2019). The configuration of the CVC feeding system (i.e. depth, shape and dimensions of the magma  
196 chambers and feeder dykes) derives from the literature (Spica et al., 2014, 2017; Massaro et al., 2018,  
197 2019) and is simplified in Figure 1d. In particular, magma chambers and dykes are considered as  
198 pressurized finite-size bodies in an elastic crustal segment, acting as fluid-filled holes. The boundary  
199 condition (pressurization) is provided by applying internal forces that act on the walls. This approach  
200 has been used extensively in several analytical and numerical models that treat magma reservoirs as  
201 internally pressurized ellipsoidal cavities within an elastic half-space, in order to gain insight into the  
202 behaviour of magma plumbing systems (Pinel and Jaupart, 2004; Gudmundsson, 2006; Grosfils, 2007;  
203 Andrew and Gudmundsson, 2008; Hautmann et al., 2013; Currenti and Williams, 2014; Zhong et al.,  
204 2019).

205 Previously published studies indicate that differences between, and problems with, elastic models  
206 derive principally from the key role played by gravity (e.g. Lister and Kerr, 1991; Watanabe et al.,  
207 2002; Gerbault, 2012; Albino et al., 2018; Gerbault, 2012; Lister and Kerr, 1991; Watanabe et al., 2002).  
208 Some authors have argued and discussed whether or not it is appropriate or not to account for the gravity  
209 body force in models of volcanic systems (e.g. Currenti and Williams, 2014; Grosfils et al., 2015).



210 When the gravitational loading is not included in the model, the volcanic deformation results from a  
211 change with respect to a stage previously at equilibrium (e.g. Gerbault et al., 2018). In this work, we  
212 carried out simulations considering the effect of the gravitational loading in the host rock, implemented  
213 via body forces. The model initial condition has a pre-assigned lithostatic stress, whose computation,  
214 in the presence of topographical and material heterogeneities, is not trivial because it requires  
215 application of the gravity load, preserving the original non-deformed geometry of the mesh  
216 (Cianetti et al., 2012). Since due to the presence of a lithostatic stress field, the load applied at the  
217 reservoir boundaries represents a superposition of the magmatic pressure and lithostatic component.  
218 We define here the magmatic pressure as either excess pressure ( $\Delta P_e$ , magmatic minus lithostatic  
219 pressure but below the tensile strength of wall rocks) or over pressure (or driving pressure  $\Delta P_o$ , which  
220 is the magmatic pressure exceeding the tensile strength of wall rocks; Gudmundsson, 2012). The first  
221 pertains to the FEMs using isolated magma chambers (single or double), while the second is used for  
222 models with connected magma chambers (with conduit/feeding system).

223 We also took into account the effect of the existing faults of the CR system even though LISA cannot  
224 include a frictional law to represent the fault movement (i.e. Chaput et al., 2014). As reported by  
225 Jeanne et al. (2017 and reference therein), the damage induced by faults increases from the host rocks  
226 to the fault core, implying a reduction in the effective elastic moduli. In this light, we represented  
227 the faults bordering the CR as two damage zones (ca. 70° of inclination, ca. 1 km thick, and down to  
228 10 km of depth) showing reduced elastic properties with respect to the surrounding host rocks.

229 To take into account the effect of the far-field extensional regime, we applied a uniform stress of 5  
230 MPa to the lateral boundaries of the domain (as reported by Martí and Geyer, 2009).

231 Considering the E–W cross-section (a–a'; Fig. 1a), we provided six domain configurations: i) a  
232 “*homogeneous lithology model*” in which the volcanic domain is only composed of andesite rocks;  
233 ii) a “*non-homogeneous lithology model*” where different geological units are considered; iii) a  
234 “*single magma chamber model*” composed of a non-homogeneous lithology and a 15 km-deep magma  
235 chamber with non-homogeneous lithology; iv) a “*dual magma chamber model*” composed of a non-

236 -homogeneous and 6 km- and 15 km-deep magma chambers; v) a “conduit feeding system model”  
237 composed of non-t homogeneous *lithology*, 6 km- and 15 km-deep magma chambers connected  
238 through a deep dyke evolving into a shallow conduit near the surface; vi) ) an “extensional model”,  
239 with a 5 MPa horizontal extensional stress (far field); and, vii) a “faulted model”, in which are also  
240 added two damaged zones mimicking the CR faults (local stress) are also added (Fig. 1b).

241 The number of nodes is set at 4426 for the only substratum and single magma chamber models, at 4161  
242 for the dual magma chamber model and at 3737 for the conduit feeding system and faulted models.

243 It is important to note that simulation outputs are shown using different colour scales. Although such a  
244 choice may make difficult visual comparison of the different runs difficult, it preserves the necessary  
245 details of stress distribution, which would have been lost using a common colour scale.

246 Finally, in the following we refer to  $\sigma_1$  as the greatest compressive stress and  $\sigma_3$  as the least compressive  
247 stress.

248

249

## 250 **4 Geological data**

251

### 252 *4.1 Stratigraphy and rock mechanics*

253 Four units forming the CVC system are defined from the available geological data (Table 2):

254 i) basement (Unit B): Cretaceous limestones and intrusive rocks forming the bed-rock underlying the  
255 CVC; ii) graben fill deposits (Unit GF): Quaternary alluvial, colluvial, and lacustrine deposits filling  
256 the graben; iii) Fuego de Colima deposits (Unit FC): andesitic lavas and pyroclastic deposits forming  
257 the Paleofuego—Fuego de Colima edifices; and iv) Volcaniclastic deposits (Unit VD): volcaniclastic  
258 deposits covering the southern flank of the CVC (e.g. Cortés et al., 2010; Norini et al., 2010, 2019).

259 We assumed constant mechanical characteristics within each unit using the typical rock mass properties  
260 of density ( $\rho$ ), Young modulus (E) and Poisson ratio ( $\nu$ ) (Table 2). The rock masses are considered dry,

261 in order for (eventual) pore pressure to be neglected. Only for Unit GF was a higher value for the  
262 Poisson ratio used close to the surface in order to mimic the high water content in the graben sediments.  
263 The maximum thickness of the graben fill (about 1 km) is assumed from the literature (Allan, 1985;  
264 Serpa et al., 1992; Norini et al., 2010, 2019). For Units B and GF, rock mass properties are derived  
265 from Hoek and Brown (1997) and Marinos and Hoek (2000), while for volcanic materials (units FC  
266 and VD; Table 2) they are estimated according to the approach proposed by Del Potro and Hürliemann  
267 (2008). In order to describe the effects of the CR faults on stress field distribution, the mechanical  
268 properties are locally degraded in proximity to the faults themselves.

269

#### 270 *4.2 Geometry of the plumbing system*

271 In our 2D model, we assume the CVC is composed of two magma chambers connected by dykes and  
272 to the surface by a conduit (Fig. 1d). The shape of the magma chambers and dykes is represented by  
273 elliptical cross-sections with the major axis ( $2a$ ) and minor axis ( $2b$ ) axes.

274 Generally, magma chambers have a sill-like shape that is often imaged in seismic studies of volcanoes  
275 and rift zones (Macdonald, 1982; Sinton and Detrick, 1992; Mutter et al., 1995; MacLeod and  
276 Yaouancq, 2000; Singh et al., 2006; Canales et al., 2009). Most of them are not totally molten but rather  
277 a mixture of melt and crystal mush (i.e. Parfitt and Wilson, 2008). Various estimates have been made  
278 to infer the actual amount of melt in a magmatic body, showing that it is only ca. 10% of the total  
279 chamber volume (Gudmundsson et al., 2012 and reference therein).

280 After Spica et al. (2017), the 15 km-deep LVB is ca. 7000 km<sup>3</sup>; therefore, if we assume the melt as  
281 10% melt, the deep magma chamber volume would be ca. 700 km<sup>3</sup>. Simplifying this volume in an  
282 elliptical sill-like geometry, the magma chamber dimensions (i.e.  $2a$ ,  $2b$  and  $2c$  axes) have to be scaled  
283 according to the LVB (55 × 30 × 8 km; Spica et al., 2017) using  $2a = 14$  km,  $2b = 3.6$  km and  $2c = 26$   
284 km,  $2c$  being elongated in an NW–SE direction. For the shallow part of the feeder system, we have no  
285 detailed geophysical constraints. However, Massaro et al. (2019) reproduced through numerical

286 modelling the nonlinear cyclic eruptive activity at Fuego de Colima in the last 20 years, using a shallow  
287 magma chamber volume in the range of 20–50 km<sup>3</sup>, according to the estimation of Cabrera-Gutiérrez  
288 and Espíndola (2010). Here we assume a volume of 30 km<sup>3</sup>, using  $2a = 3.5$  km,  $2b = 2$  km and  
289  $2c = 8$  km as the dimensions of the shallow magma chamber.

290 Numerous theoretical and field studies have established that host rock stresses dictate the magma  
291 pathways (e.g. Gudmundsson, 2011; Maccaferri et al., 2011, 2011). During ascent to the surface, the  
292 dykes align themselves with the most energy-efficient orientation, which is roughly perpendicular to  
293 the least compressive stress (e.g. Gonnermann and Taisne, 2015; Rivalta et al., 2019), providing the  
294 magma driving pressure remains small compared to the deviatoric stress (Pinel et al., 2017; Maccaferri  
295 et al., 2019). This behaviour, however, can be modulated in the presence of significant variations in  
296 the fracture toughness of the surrounding rock due to stratification (Maccaferri et al., 2010) or to old  
297 and inactive fracture systems (Norini et al., 2019).

298 Although for oblate magma chambers the propagation of dykes is most probable from the tip areas, in  
299 our simulations the orientation of dykes is assumed to be vertical, because of the preferential pathways  
300 represented by the CR fault planes (Spica et al., 2017).

301 We set the dimensions of the feeder dykes in agreement with Massaro et al. (2018): deep dyke  $2ad =$   
302 2 km; shallow dyke  $2a$  varies from 1 km at the bottom to 500 m in the upper part of the volcano; width  
303 of both deep and shallow dykes  $2bd = 2b = 100$  m (Fig. 1d).

304 It is worth noting that it is outside the scope of this work to provide the conditions for rupture of the  
305 magma chamber, LISA accounting only for the elastic regime. For these reasons, we fixed  $\Delta P_e$  and  
306  $\Delta P_o$  (for isolated and connected magma chamber models, respectively) in the range of 10–20 MPa  
307 for the 15 km-deep chamber, and 5 MPa for the 6 km-deep one. For the dykes and conduit,  $\Delta P_o$  is set  
308 to 10 MPa in the deeper dyke and 5 MPa in the shallower one, while in the upper 500 m of conduit it  
309 is 0.4 MPa.

## 310 **Results**

311

312 In this section, we report the sensitivity analysis carried out to quantify approximation of the Young  
313 modulus variation on FEM outputs, and description of the model outputs when adding complexity to  
314 the input geological/geophysical data.

315

### 316 *5.1 Sensitivity analysis of Young modulus*

317 Using the single magma chamber model as a reference case, we quantified the influence of Young  
318 modulus variation in each geological unit. Taking into account the mechanical properties of rocks  
319 (Table 2) as reference values, we compared the stress state of the computational domain on changing  
320 Young modulus by ( $\pm$ ) one order of magnitude. This sensitivity analysis, although incomplete, may  
321 lead to raised awareness on the selection of input data when running an FEM. The sensitivity analysis  
322 was carried out on a reduced simulation domain (the  $x$ -axis was set to 35 km) in order to diminish the  
323 influence of binding effects along the domain borders.

324 We applied the Euclidean norm (L2) method to illustrate the results. The L2 norm applied on a vector  
325 space  $x$  (having components  $i = 1, \dots, n$ ) is strongly related to the Euclidean distance from its origin,  
326 and is equal to:

327

$$328 \quad ||x||_2 = \sqrt{\sum_i^n x_i^2} \quad (1)$$

329

330 In our case, the vector space  $x$  is composed of all nodes of the computational domain (Table 1). We  
331 defined  $x_{ref}$ , the vector containing the results for the maximum and minimum principal stress, when  
332 using the selected values of material properties (Table 1) and  $x(-)$  and  $x(+)$ , the vectors on varying the  
333 Young modulus by one order of magnitude in each unit.

334 In Figure 2 are reported the global relative variations in L2 of  $\sigma_1$  and  $\sigma_3$  caused by the variation of  
335 Young modulus in each unit, for each model configuration (i.e. non-homogeneous lithology, single  
336 magma chamber, dual magma chamber and dual magma chamber with conduits models) as follows:

337

$$338 \quad \|x\|_{2(-)} = \|x_{\text{ref}} - x_{(-)}\|_2 / \|x_{\text{ref}}\|_2 \quad (2)$$

$$339 \quad \|x\|_{2(+)} = \|x_{\text{ref}} - x_{(+)}\|_2 / \|x_{\text{ref}}\|_2 \quad (3)$$

340

341 All the models show variability of less than 15%, with a few exceptions within Unit B that have  
342 variability of over 30% (Fig. 2). In this light, the spatial distribution of the major variations seems not  
343 to significantly affect the final stress distributions, because: i) they are located near the mesh borders  
344 (Fig. 3a and b); and ii) when not at the mesh borders, the variations are limited to a few % (Fig. 3c  
345 and d). It means that a one order of magnitude variation in Young modulus produces variation in FEM  
346 outputs distributed over a large domain, and the change affecting the single nodes is limited to a few %.

347

## 348 *5.2 Homogeneous and non-homogeneous lithology*

349 In Figure 4 we report  $\sigma_1$  and  $\sigma_3$  stresses for gravity-loaded models with homogeneous lithology  
350 composed of only andesitic lavas (Fig. 4a) and non-homogeneous lithology composed of carbonates  
351 (Unit B) and alluvial, volcanoclastic and pyroclastic deposits (Units GF and VD; Fig. 4b). It is  
352 important to stress that the  $x$ - $z$  zero displacement assigned at the bottom and at the lateral boundaries  
353 of the domain created substantial artefacts in the results (i.e. curved patterns of stress), especially  
354 considering  $\sigma_3$  (Fig. 4, panels i and ii) where the boundary effect on the  $x$ -axis is amplified by the  
355 presence of the upper free surface. It follows that the only unperturbed area extends ca. 30 km  
356 horizontally and ca. 15 km vertically (within the blue contour in Fig. 4). It is worth noting that the  
357 homogeneous and non-homogeneous models show quite similar stress patterns results (Fig. 4).

358

### 359 5.3 Gravitational modelling using inferred feeding system geometry

360 In Figures 5 and 6 we show three cross-section profiles describing the feeding system starting from a  
361 single magma chamber to two chambers, then adding the conduits and, finally, considering the full  
362 complexity by adding the effects of far-field stress and CR faults. Figure 5a describes  $\sigma_3$  (panel i) and  
363  $\sigma_1$  (panel ii) stress distribution for the single magma chamber model and  $\Delta P_e = 10$  MPa. No significant  
364 differences in the magnitude and pattern of stresses are visible using  $\Delta P_e = 20$  MPa (Appendix 1a).

365 The addition of the shallow magma chamber significantly changes the values and pattern of both  $\sigma_3$   
366 and  $\sigma_1$  (Fig. 5b). In particular,  $\sigma_3$  and  $\sigma_1$  stresses describe a typical inflation pattern produced by excess  
367 pressure in the magma chamber(s) (Anderson, 1936; Gudmundsson, 2006, 2012), producing well-  
368 defined stress arches of  $\sigma_3$  (red dotted lines in Fig. 5bi) and divergent strong gradients of  $\sigma_1$  around the  
369 deep magma chamber (Fig. 5bii). Very slight differences in the magnitude and pattern of stresses  
370 appear when using  $\Delta P_o = 10$  MPa (Fig. 5b) or 20 MPa (Appendix 1b).

371 Looking at Figure 6, it is evident how insertion of the conduits in the CVC feeding system dramatically  
372 changes the stress distribution, with the disappearance of the stress arch and a nearly constant stress in  
373 the computational domain except around the deep magma chamber tips.

374

### 375 5.4 Application of an extensional stress field

376 In order to explore the influence of extensional far-field stress on stress patterns (Fig. 1a), we ran  
377 simulations applying 5 MPa stress (typical low value for rift zones; Turcotte and Schubert, 2002;  
378 Moeck et al., 2009; Maccaferri et al., 2014; Sulpizio and Massaro, 2017) along the lateral boundaries  
379 of the computational domain (Fig. 7).

380 In the case of a single magma chamber ( $\Delta P_e = 10$  MPa; Fig. 7, panels i and- ii), the addition of the far-  
381 field stress reduces the confinement effect due to the no displacement condition imposed along the  $x$ -  
382  $-z$  directions (plane strain approximation). When considering the double magma chamber  
383 configuration ( $\Delta P_o = 10$  MPa in the deep chamber and  $\Delta P_o = 5$  MPa in the shallower one), the presence

384 of the far-field stress produces slight changes in stress magnitude and pattern for both  $\sigma_3$  and  $\sigma_1$  (Fig.  
385 7, panels iii and iv) with respect to Figure 5b. Very similar effects appears ion the complete feeding  
386 system configuration model (Fig. 7, panels v and -vi). Also, in this case using  $\Delta P_o = 20$  MPa in the  
387 deep magma chamber does not significantly affect the model outputs (Appendix 2).

388

### 389 *5.5 Faults bordering the Colima Rift*

390 The effect of faults bordering the CR on the final feeding system configuration is simulated through  
391 two damage zones by degrading their elastic properties. Adding these elements does not significantly  
392 alter the stress distribution observed in Figures 7v and 7vi, but only provides a slight reduction in both  
393  $\sigma_1$  and  $\sigma_3$  intensities around their edges (Figs. 7vii and 7viii). The different distance of the two damage  
394 zones from the feeding system produces a small asymmetry in both  $\sigma_1$  and  $\sigma_3$  patterns with respect to  
395 simulations without damage zones, especially near the deep magma chamber (Figs. 7v–viii).

396

397

## 398 **6 Discussion**

399

### 400 *6.1 FEM analysis at increasing geological detail*

401 This study highlights some important features of crustal stress distribution on changing the geological  
402 and geophysical constraints as input conditions (Spica et al., 2014, 2017; Massaro et al., 2018).  
403 Although the results have to be considered as a first-order approximation, the changes in stress  
404 distribution are appreciable and useful for a better understanding of the limitations and advantages of  
405 FEM.

406 Under the assumptions of plane strain and gravitational loading, the use of homogeneous or non-  
407 homogeneous lithology provides negligible effects in stress intensity and pattern (Fig. 4). This is likely



408 due to the limited thickness of the shallow units (Units FC, VD and, GF; Table 2) in the simulated  
409 domain, which the results of which are dominated by Unit B (Table 2). However, this does not mean  
410 that the influence of the upper units may be still negligible using smaller scales of the simulated domain.  
411 Analysing the single magma chamber model outputs, it emerges how  $\Delta P_e$  limits the effects of  
412 gravitational loading. On the contrary, the dual magma chamber geometry better describes the inflation  
413 induced by  $\Delta P_e$  within magma chambers, with the formation of the stress arch in the  $\sigma_3$  plot. It is  
414 worth noting that for both single and dual magma chamber models, changing  $\Delta P_e$  from 10 to 20 MPa  
415 slightly affects the magnitude of the stress but not its general pattern (Appendices 1 and 2).  
416 The presence of dykes in the magma feeding system dramatically changes the  $\sigma_3$  and  $\sigma_1$  patterns (Fig. 6),  
417 which become quite homogeneous throughout the computational domain, with the only exception of  
418 sidewall effects induced by the zero displacement conditions.  
419 The addition of extensional field stress of 5 MPa reduces the sidewall effects and produces an almost  
420 homogeneous stress distribution in the upper part of the computational domain, above the top of the  
421 deep magma chamber. This, along with the additional inclusion of the damage zones introduced to  
422 mimic the effects of CR faults, describes a volcanic system close to equilibrium, in which pressure  
423 within the volcano feeding system almost equilibrates the lithostatic stress (Sulpizio et al., 2016).

## 424

### 425 *6.2 Some implications of the stress state of the CVC inferred from FEM*

426 The results from the most complete FEM runs highlight an almost homogeneous stress distribution in  
427 the CVC area. This means the dual magma chamber model and the application of far-field stress  
428 provide a stable geometry, which limits the stress changes to a few MPa. The majority of stress  
429 variations are located at the tips of the magma chambers, as expected for pressurized or under-  
430 pressurized cavities in the lithosphere (Martí and Geyer, 2009), implying that the whole feeding system  
431 is in a quasi-equilibrium state. Even if we consider the scenario of complete emptying of the upper  
432 conduit and part of the shallow magma chamber, as occurred occasionally during the past sub-Plinian

433 and Plinian eruptions (Luhr et al., 2002; Saucedo et al., 2010; Massaro et al., 2018), this would result  
434 in the restoration of the stress arch, which is still a stable stress configuration. Even complete emptying  
435 of the shallow magma chamber would probably be ineffective for triggering a large collapse (caldera-  
436 forming) of the feeding system.

437 Beside and beyond the limitations due to the first-order approximation of the FEM analysis, other  
438 sources of uncertainty in the discussion about the present and future stress state of the CVC come from  
439 not considering gravity-driven processes, such as volcano spreading due to plastic deformation of Unit  
440 GF (Norini et al., 2010, 2019) and detailed regional tectonics (Norini et al., 2010, 2019). The effect of  
441 the two fault systems bordering the CR is here simulated by degrading the mechanic properties of rocks  
442 in an area of about 1 km width up to a depth of 10 km. Although the effects are negligible at the scale  
443 of the computational domain, it cannot be excluded that some local significant effects that cannot be  
444 resolved using the described approach.

445

## 446 **7 Summary and conclusion**

447 The presented study highlights the importance of using complete and detailed geological and  
448 geophysical data when dealing with FEM of volcanic areas. The different geological detail used in the  
449 model runs showed how the stress pattern depends critically on the geometry of the volcano feeding  
450 system, with huge differences in having a single or double magma chamber system and, in particular,  
451 whether or not the magma chamber(s) are connected to the surface by feeder dykes and conduits. The  
452 geometry of the feeding system is prevalent on model outputs with respect to varying rock properties  
453 (i.e. Young modulus) of one order of magnitude. In the case of CVC, the use of subsurface  
454 homogeneous or stratified lithology does not influence the FEM outputs much, the subsurface geology  
455 of the computational domain being dominated by carbonates (Unit B).

456 Beside and beyond the results obtained by analysing the influence of detailed geological and  
 457 geophysical data, the presented modelling confirms the close to equilibrium state of the volcano, which  
 458 is the expected stress distribution induced by a feeding system directly connected to the surface.  
 459 The Complete emptying of the upper conduit and part of the shallow magma chamber, as occurred  
 460 occasionally in the past, originating sub-Plinian and Plinian eruptions, would result in restoration of  
 461 the stress arch, which is still a stable stress configuration. It follows that large magnitude, caldera-  
 462 forming eruptions are possible only if the bigger deep magma chamber is also involved and  
 463 significantly emptied during an eruption.

464

465 **Tables**

466

467 **Table 1** - Element types used in LISA analysis considering the final conduit feeding system  
 468 configuration – Fig.1d, panel vi)

<i>E-W cross-section (a-a')</i>		Element Type	Elements	Nodes
470	FC Fuego de Colima	quad4-tri3	372	384
471	VD Volcanic Deposits	quad4-tri3	245	273
472	GF Graben Fill	quad4-tri3	456	338
473	B Basament	quad4-tri3	3088	2907
474	CG Colima graben	quad4-tri3	48	71

475 Total Elements: 4209

476

477 **Table 2** - Rock mass and mechanical properties of the geological Units used in the finite-element model  
 478 (from Norini et al., 2010, 2019).

479

Acronym	Model Unit	Rock Type	Density (kg/m <sup>3</sup> )	Young's Modulus (MPa)	Poisson's ratio $\nu$
FC	Fuego de Colima	Andesitic lavas and pyroclastic deposits forming the Paleofuego-Fuego de Colima volcano	2242	$1.4 \times 10^3$	0.30

VD	Volcaniclastic deposits	Pyroclastic and epiclastic deposits covering the southern flank of the CVC	1539	$1.7 \times 10^3$	0.32
GF	Graben Fill	Quaternary alluvial, colluvial, lacustrine deposits filling the graben	1834	$1.5 \times 10^3$	0.35
B	Basement	Cretaceous limestones and intrusive rocks forming the bed-rock underlying the CVC	2650	$3.6 \times 10^4$	0.30

480

481

482

## 483 **Appendices**

484

### 485 **Appendix 1**

486 E–W gravitational modelling of the CVC domain (stratified lithology) for all configurations  
487 investigated. The magnitude and pattern of the principal stress account for a) single magma chamber  
488 model (4426 nodes: 4426); b) dual magma chamber model (number of nodes: 4161 nodes); c) dual  
489 magma chamber with conduits model (number of nodes: 3737 nodes). The Dimensions of the deep  
490 magma chamber:  $2a = 14$  km and  $2b = 3.6$  km at 15 km of depth; shallow magma chamber:  $2a = 3.5$   
491 km and  $2b = 2$  km at 6 km.  $\Delta P_e$  and  $\Delta P_o$  equal to= 20 MPa for the deep chamber, and 5 MPa for the  
492 shallower. Black dotted lines highlight the passage from different stress values. Note that the scales of  
493 stress values are different for each panel in order to maximize the simulation details.

494

### 495 **Appendix 2**

496 E–W gravitational modelling of the CVC domain (stratified lithology) considering an extensional far  
497 field of 5 MPa for all configurations investigated. The magnitude and pattern of the principal stress  
498 account for a) single magma chamber model (nodes: 4426 nodes); b) dual magma chamber model  
499 (number of nodes: 4161 nodes); c) dual magma chamber with conduits model (number of elements:  
500 3737 nodes). The Dimensions of the deep magma chamber:  $2a = 14$  km and  $2b = 3.6$  km at 15 km  
501 depth; shallow magma chamber:  $2a = 3.5$  km and  $2b = 2$  km at 6 km.  $\Delta P_e$  and  $\Delta P_o$  are equal to= 20  
502 MPa for the deep chamber, and 5 MPa for the shallower. Black dotted lines highlight the passage from  
503 different stress values. The Red arrows indicate the direction of the applied far-field stress. Note that  
504 the scales of stress values are different for each panel in order to maximize the simulation details.

505

## 506 **Figure Captions**

507

508 **Fig. 1** (a) Morphotectonic map of the Colima Volcanic Complex (NC = Nevado de Colima volcano;  
509 FC = Fuego de Colima volcano) and Colima Rift with the main tectonic and volcano-tectonic structures  
510 (NCG = Northern Colima Graben; CCG = Central Colima Graben, from Norini et al., 2019). Inset: the  
511 location of the Colima Volcanic Complex (CVC) within the Trans-Mexican Volcanic Belt (TMVB) is  
512 shown in the frame of the subduction-type geodynamic setting of Central America (from Davila et al.,  
513 2019); (b) general sketch of the geometrical configurations used in LISA; (c) example of mesh of the  
514 investigated area for the dual magma chamber model with conduits (case v in panel (b), considering  
515 zero displacement along the bottom and left and right sides. Note that for case (vi) in panel (b) the zero  
516 displacement is removed from the lateral sides; (d) sketch of the Fuego de Colima feeding system  
517 composed of a 15 km-deep magma chamber connected to the surface via a 6 km-deep magma chamber  
518 and dykes.  $\Delta P_{chs}$  and  $\Delta P_{chd}$  indicate either excess or over pressure (depending on the model used) in  
519 the shallow and deep chambers, respectively (modified from Massaro et al., 2019).

520

521 **Fig. 2** Results of the sensitivity analysis carried out on the Young modulus variations within each rock  
522 layer of the domain considering different configurations (stratified substratum model – 4426  
523 nodes; single magma chamber model – 4426 nodes; dual magma chamber model – 4161  
524 nodes; dual magma chamber with conduits model – 3737 nodes). For each geological unit  
525 (B, FC, GF, VD), the relative global variation in L2 (%) is provided for  $\sigma_1$  and  $\sigma_3$ . The  $x(-)$  and  $x(+)$   
526 vectors indicate the variation in Young's modulus variation by an order of magnitude with respect to  
527 the  $x_{ref}$  vector, containing the stress values calculated by using the values of the material's properties  
528 indicated in Table 2.

529

530 **Fig. 3** Spatial variation (%) of the L2 norm's components at varying Young modulus for selected cases  
531 of Units B and VD: (a) Unit B in the stratified substratum model (4426 nodes); (b) Unit B in the single  
532 magma chamber model (4426 nodes); (c) Unit B in the dual magma chamber model (4161 nodes);  
533 (d) Unit VD in the dual magma chamber with conduits model (nodes: 3737 nodes). Symbols  $x(-)$  (-)  
534 and  $x(+)$  have the same meaning as inof Figure 2.

535

536 **Fig. 4** E–W gravitational modelling of the CVC domain. The scale of the mesh is expressed in units of  
537 design (1 UD = 1 km). The domain extends 60 km along the  $x$ -axis, and 30 km along the  $z$ -axis. The  
538 number of nodes used in the mesh is set to 4426. The magnitude and pattern of the principal stresses  
539 (dotted black lines) are reported for (a) homogeneous stratigraphy (Unit FC = andesitic lavas and  
540 pyroclastic deposits) and (b) non-homogeneous stratigraphy (Unit FC; Unit B = Cretaceous limestone  
541 and intrusive rocks forming the bedrock underlying the CVC; Unit GF = Quaternary alluvial, colluvial  
542 and lacustrine deposits filling the graben; Unit VD = volcaniclastic deposits covering the southern flank  
543 of the CVC). The blue line contours the unperturbed part of the domain, which extends ca. 30 km  
544 horizontally and ca. 25 km vertically. Note that the scale of stress values is the same for all simulations.

545

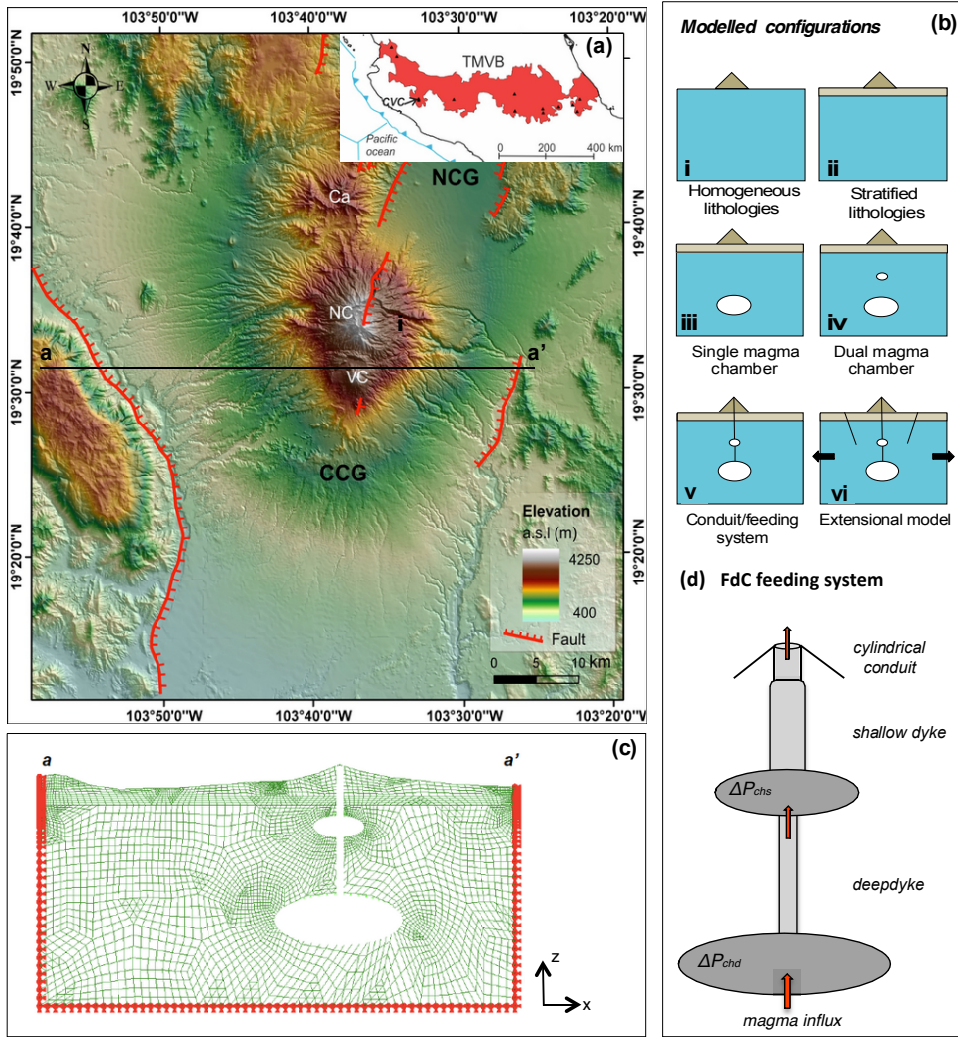
546 **Fig. 5** E–W gravitational modelling of the CVC domain with non-homogeneous stratigraphy. The  
547 magnitude and pattern of the principal stresses are reported for (a) the single magma chamber model  
548 represented by a magma chamber ( $2a = 14$  km and  $2b = 3.6$  km) at 15 km depth, and (b) the dual  
549 magma chamber model composed of a 15 km-deep magma chamber ( $2a = 14$  km and  $2b = 3.6$  km) and  
550 a shallow 6 km-deep one ( $2a = 3.5$  km and  $2b = 2$  km). The magma chambers are not connected.  $\Delta P_o$   
551 is set to 10 and 5 MPa for the 15 km-deep and 6 km-deep magma chambers, respectively. The number  
552 of nodes is set to 4426 and 4161 for the single and dual magma chamber models, respectively. Black  
553 dotted lines highlight the passage from different stress values. The red dotted line in panel (bi) indicates  
554 the formation of the stress arch. Note that the scale of stress values is different for each panel in order  
555 to maximizse the simulation details.

557 **Fig. 6** E–W gravitational modelling of the CVC domain with non-homogeneous stratigraphy  
558 accounting for a dual magma chamber system connected by dykes via the surface (deep magma  
559 chamber,  $2a = 14$  km and  $2b = 3.6$  km at 15 km depth; shallow magma chamber,  $2a = 3.5$  km and  $2b =$   
560  $= 2$  km at 6 km od depth). The magnitude and pattern of the principal stresses are shown. The number  
561 of nodes used is set to 3737.  $\Delta P_o$  is set to 10 and 5 MPa for the 15 km-deep and 6 km-deep magma  
562 chambers, respectively. The black dotted lines in panel (ii) highlight the passage from different stress  
563 values. Note that the scale of stress values are is different for each panel in order to maximizse the  
564 simulation details.

566 **Fig. 7** E–W gravitational modelling of the CVC domain with non-homogeneous stratigraphy  
567 considering the extensional field stress. The magnitude and pattern of the principal stresses are shown  
568 for the single magma chamber model (panels i and -ii), the dual magma chamber model (panels iii and-  
569 iv) and, the dual magma chamber with conduits model (panels v-vi-vii–viii). Note that in panels vii  
570 and -viii the faults bordering the CG are shown. For all configurations, an extensive far-field stress of  
571 5 MPa is applied at the lateral boundaries of the domain. In panels vii and- viii, the additional effect of  
572 the local extensive field is simulated using a reduced values of material properties (Table 2).  $\Delta P_o$  is set  
573 to 10 and 5 MPa for the 15 km-deep and 6 km-deep magma chambers, respectively. Black dotted lines  
574 highlight the passage from different stress values. The red arrows indicate the direction of the applied  
575 far- field stress. Note that the scale of stress values is different for each panel in order to maximizse the  
576 simulation details.

577

578 Figure 1



579

580

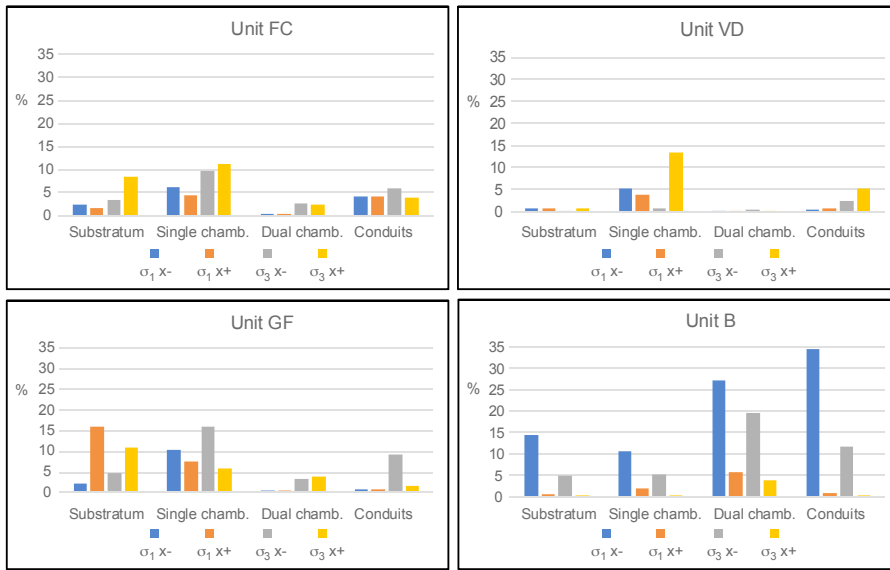
581

582

583

584

585 Figure 2



586

587

588

589

590

591

592

593

594

595

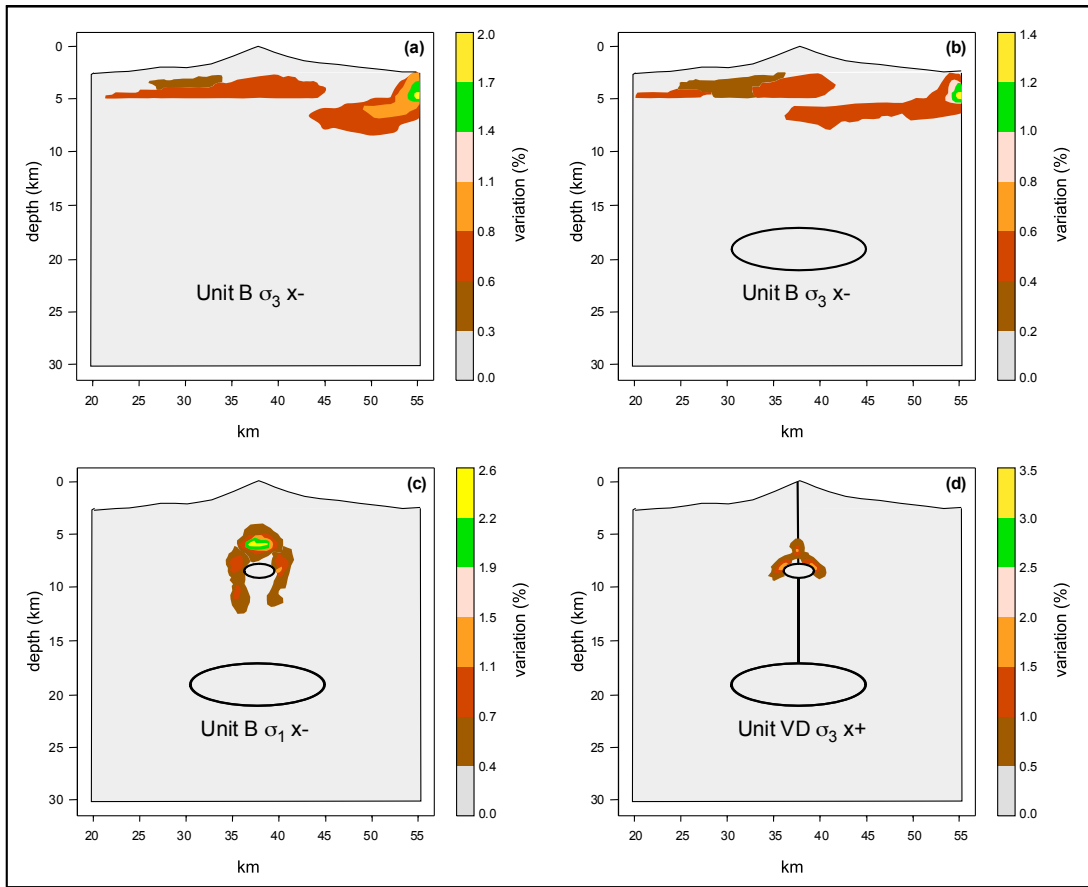
596

597

598

599 Figure 3





600

601

602

603

604

605

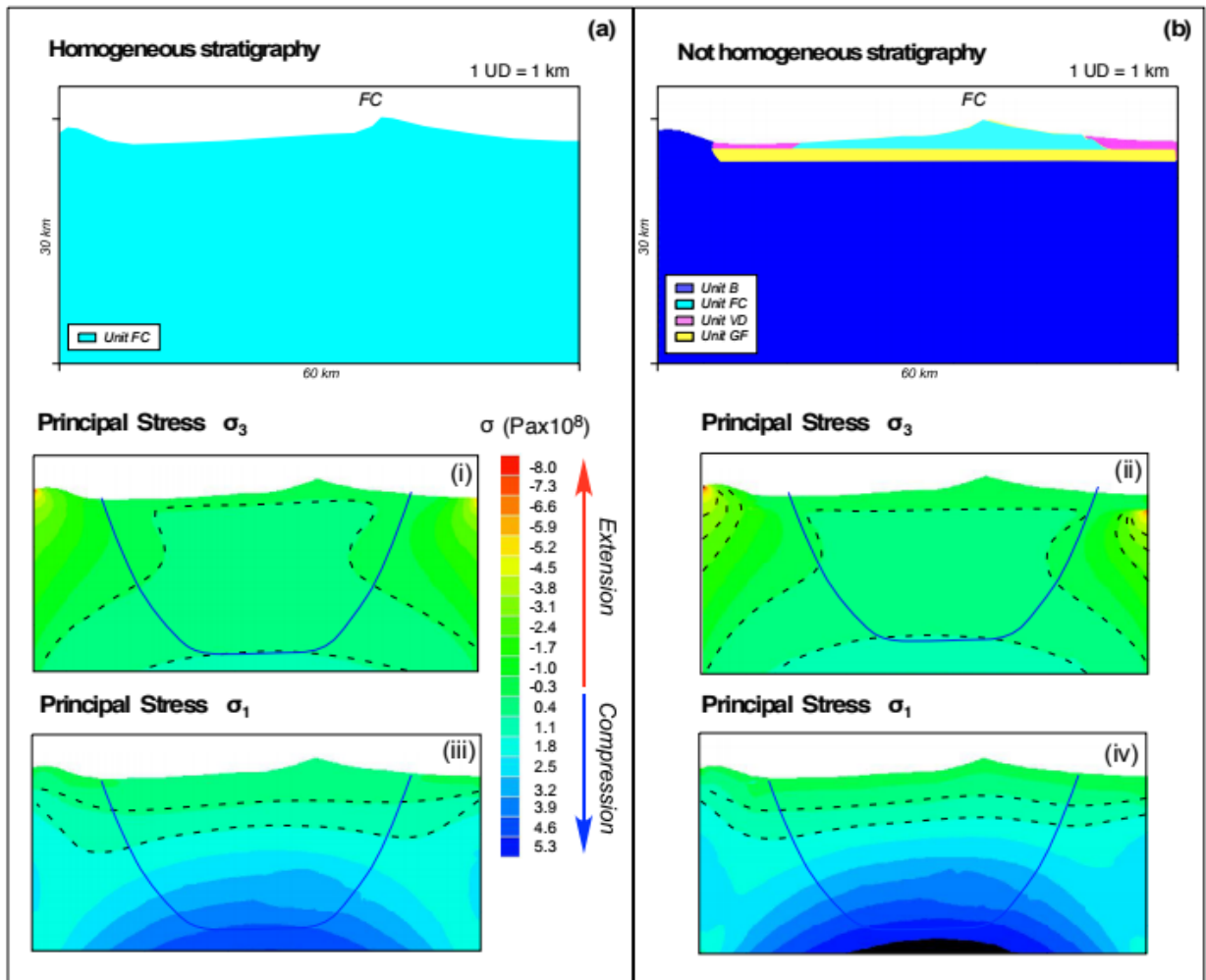
606

607

608

609 Figure 4

610



611

612

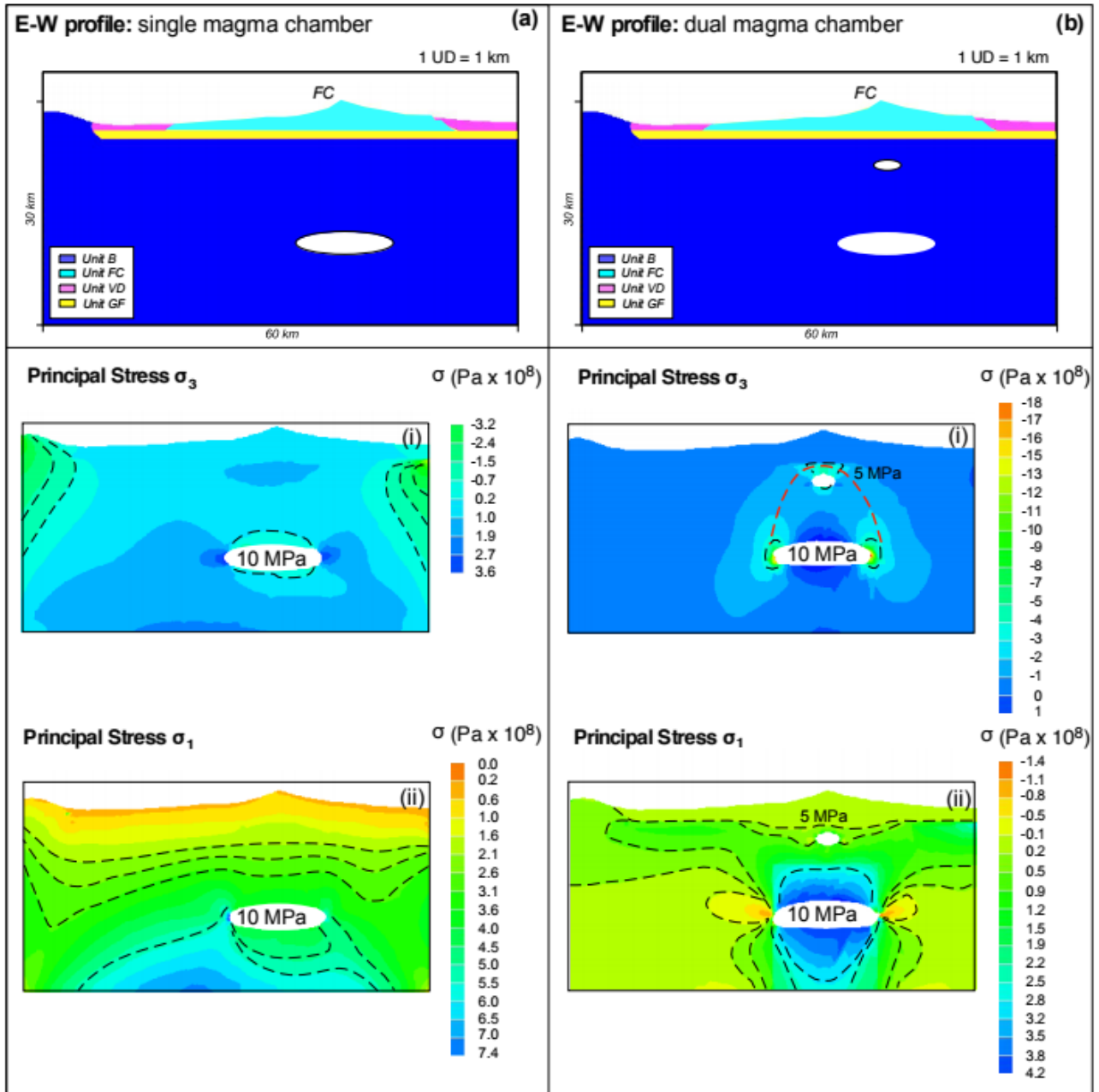
613

614

615

616

617 Figure 5



618

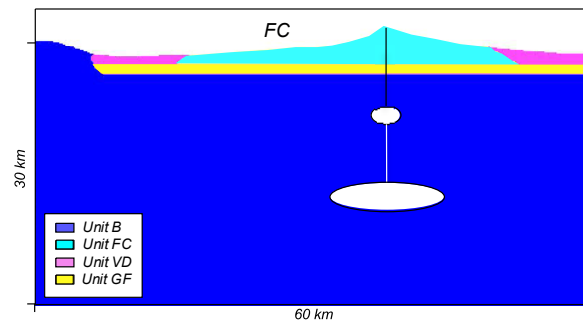
619

620

621

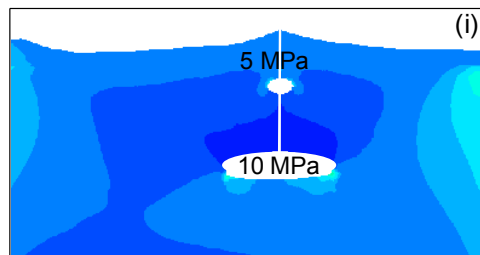
622 Figure 6

**E-W profile: conduits and magma chambers**



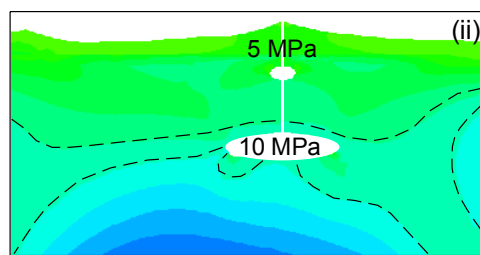
**Principal Stress  $\sigma_3$**

$\sigma$  (Pa x  $10^8$ )



**Principal Stress  $\sigma_1$**

$\sigma$  (Pa x  $10^8$ )



623

624

625

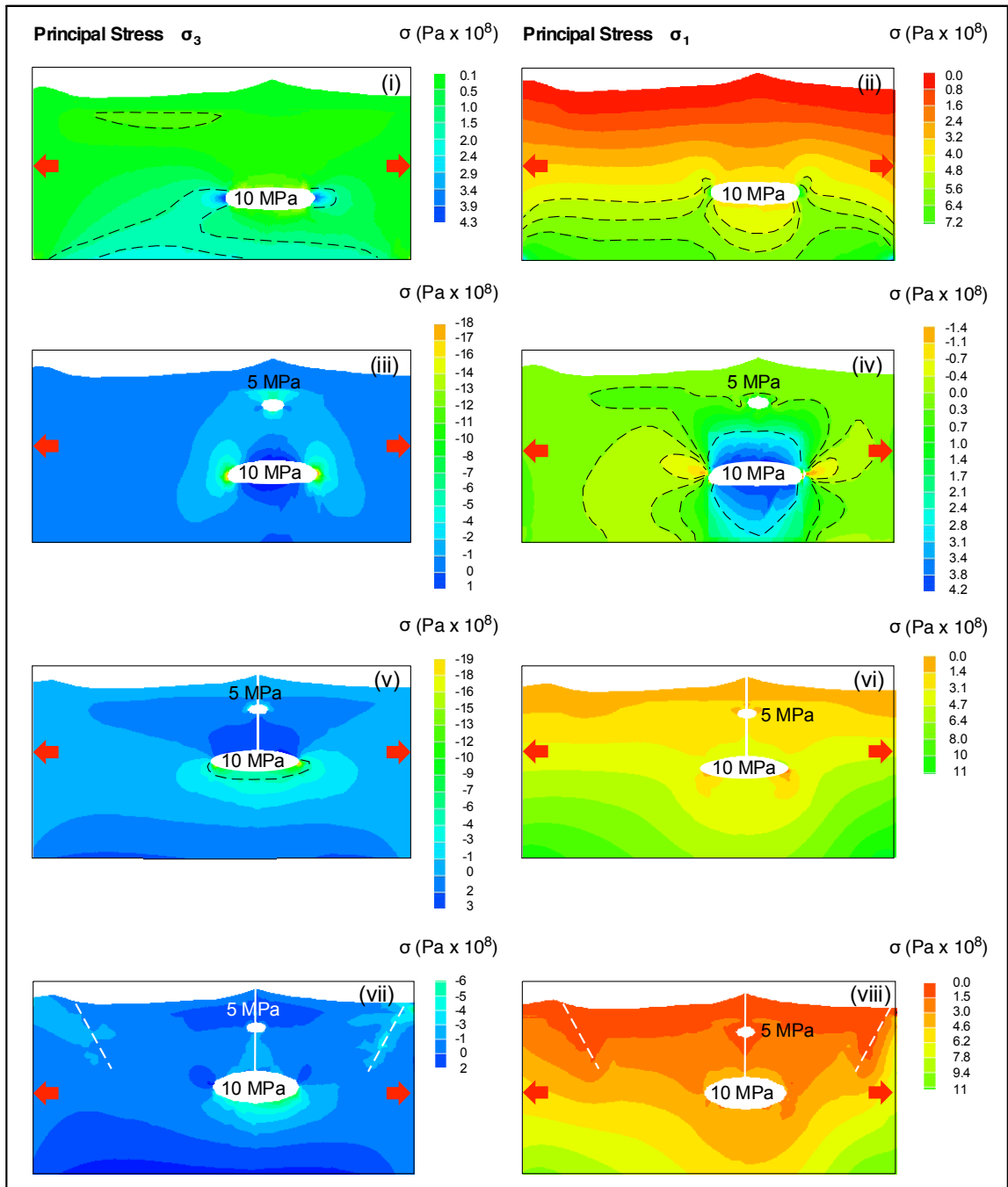
626

627

628

629

630 Figure 7



631

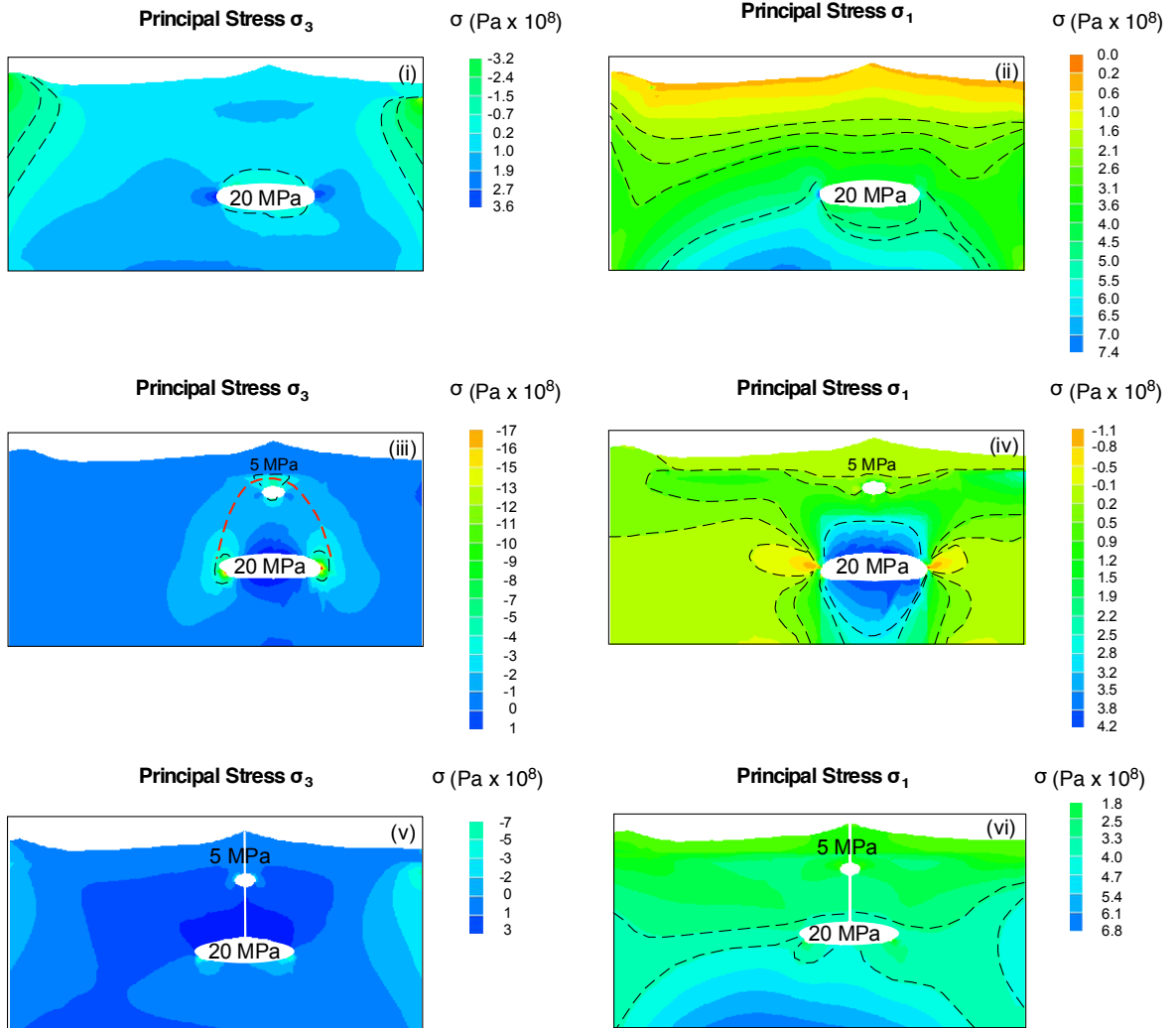
632

633

634

635 Appendix 1

# Appendix 1



636

637

638

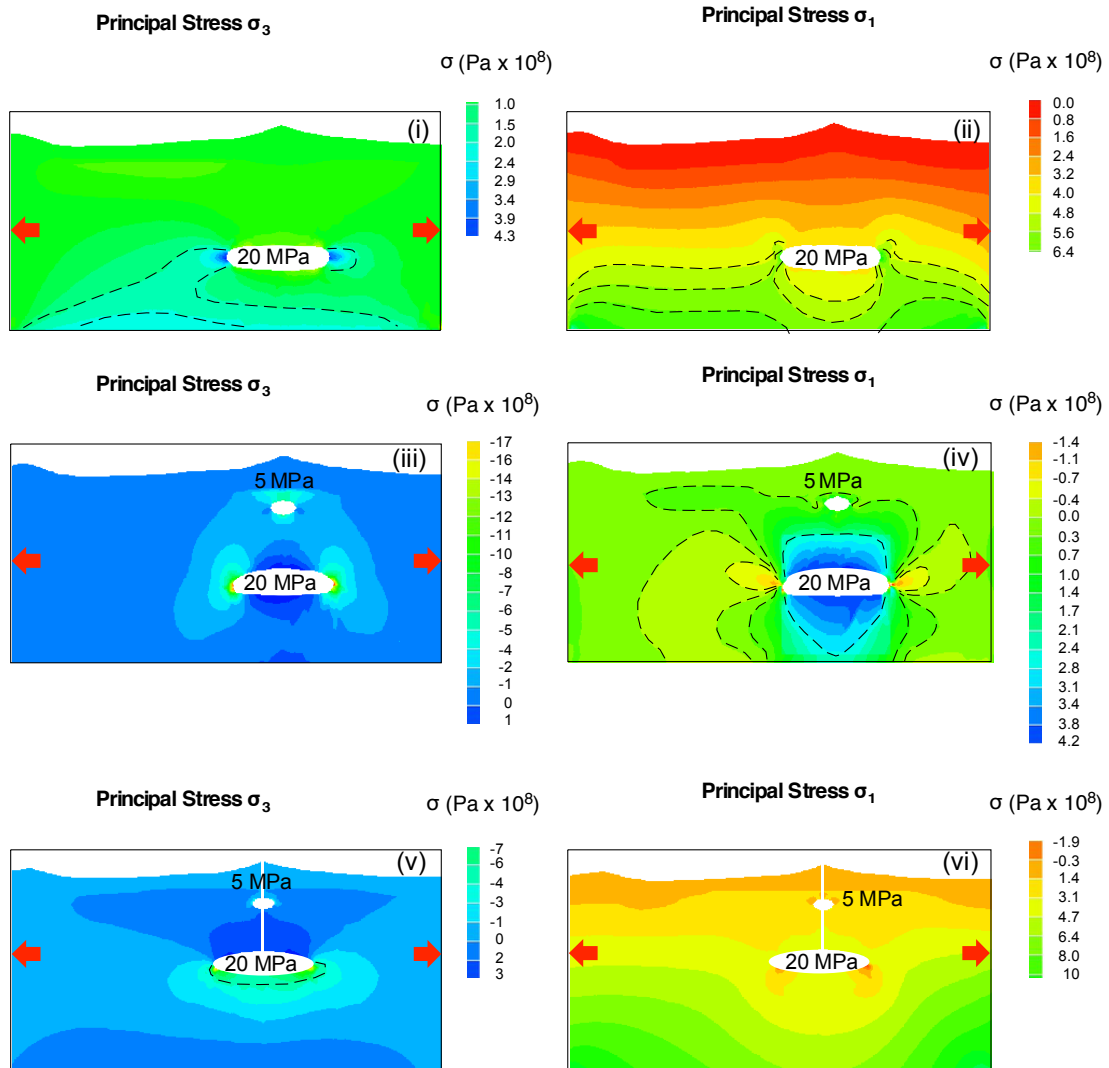
639

640

641

642 Appendix 2

## Appendix 2



643

644

### 645 Code/Data Availability

646 The LISA code is available at <https://lisafea.com/>.

647

### 648 Author's contribution

649 SM, RS, AC, GN and GG conceived the study. SM and RS wrote the bulk of the manuscript with the  
650 input of all the co-authors. SM and GL compiled the numerical simulations and formulated the adopted  
651 methodology. MP and SM carried out the sensitivity analysis. All authors worked on the interpretation

652 of the results.

653

654 **Competing interests:** The authors declare that they have no conflict of interest.

655

656 **Acknowledgements:** The manuscript received a professional copy-editing. SM thanks the LISA  
657 customer service for the support received. In particular, Karl.

658

## 659 **References**

660 Albino, F., Pinel, V., and Sigmundsson, F., 2010. Influence of surface load variations on eruption  
661 likelihood: application to two Icelandic subglacial volcanoes, Grímsvötn and Katla. *Geophysical*  
662 *journal international*, 181(3), 1510-1524.

663

664 Albino, F., Amelung, F., and Gregg, P., 2018. The role of pore fluid pressure on the failure of magma  
665 reservoirs: insights from Indonesian and Aleutian arc volcanoes. *Journal of Geophysical Research:*  
666 *Solid Earth*, 123(2), 1328-1349.

667

668 Anderson E.M., 1936. The dynamics of formation of cone sheets, ring dykes and cauldron subsidence.  
669 *Proc R Soc Edinburgh* 56:128–163.

670

671 Allan, J.F., 1985. Sediment depth in the NCG from 3-D interpretation of gravity. *Geofis. Int.* 24, 21–  
672 30 (1985).

673 Allan, J.F. 1986. Geology of the Northern Colima and Zacoalco grabens, Southwest Mexico: Late  
674 Cenozoic rifting in the Mexican Volcanic Belt. *Geol. Soc. Am. Bull.* 97, 473–485

675 Allan, J.F., Nelson, S.A., Luhr, J.F., Charmichael, I.S.E., Wopat, M., Wallace, P.J., 1991: Pliocene-  
676 Holocene rifting and associated volcanism in Southwest Mexico: an exotic terrane in the making. In:  
677 Dauphin, J.P., Simoneit, R.R.T. (eds.) *The Gulf and Peninsular Provinces of the Californias*, AAPG  
678 *Mem.*, vol. 47, pp. 425–445.

679 Andrew, R.E., and Gudmundsson, A., 2008. Volcanoes as elastic inclusions: Their effects on the  
680 propagation of dykes, volcanic fissures, and volcanic zones in Iceland. *Journal of Volcanology and*  
681 *Geothermal Research*, 177(4), 1045-1054.

682

683 Arámbula-Mendoza, R., Reyes-Dávila, G., Dulce, M.V.B., González-Amezcuca, M., Navarro- Ochoa,  
684 C., Martínez-Fierros, A., and Ramírez-Vázquez, A., 2018. Seismic monitoring of effusive-explosive  
685 activity and large lava dome collapses during 2013–2015 at Volcán de Colima, Mexico. *J. Volcanol.*  
686 *Geotherm. Res.*, 351, 75-88.

687 Babuška, I., Ihlenburg, F., Paik, E. T., and Sauter, S.A., 1995. A generalized finite element method  
688 for solving the Helmholtz equation in two dimensions with minimal pollution. *Computer methods in*  
689 *applied mechanics and engineering*, 128(3-4), 325-359.

690

691 Bandy, W.L., Mortera-Gutiérrez, C.A., Urrutia- Fucugauchi, J., Hilde, T.W.C, 1995. The subducted  
692 Rivera-Cocos plate boundary: where is it, what is it, and what is its relationship to the Colima Rift?



- 693 Geophys. Res. Lett. 22, 3075–3078.
- 694 Barrier, B., Bourgois, J., Michaud, F., 1990: The active Jalisco triple junction rift system. C.R. Acad.  
695 Sci. Paris, 310 (II), 1513–1520.
- 696 Bathe, K. J., Zhang, H., and Ji, S., 1999. Finite element analysis of fluid flows fully coupled with  
697 structural interactions. Computers and Structures, 72(1-3), 1-16.
- 698
- 699 Bonafede, M., Parenti, B., Rivalta, E., 2002. On strike-slip faulting in layered media. Geophysical  
700 Journal International, 149(3), 698-723.
- 701
- 702 Bonasia R, Capra L, Costa A, Macedonio G, Saucedo R., 2011. Tephra fallout hazard assessment for  
703 a Plinian eruption scenario at Volcan de Colima. J Volcanol Geotherm Res 203: 12–22.
- 704
- 705 Borelli, A.P., Schmidt, R.J., and Sidebottom, O.M., 1985. Advanced mechanics of materials (Vol. 6).  
706 New York et al.: Wiley.
- 707
- 708 Buchmann T. and Conolly P.T., 2007. Contemporary kinematics of the Upper Rhine Graben: A 3D  
709 finite element approach. Global and Planetary Change 58, 287–309.
- 710
- 711 Bunney, 2014. The Effects of Structural Heterogeneities and In-elastic Rheology on Ground  
712 Deformation at Campi Flegrei Caldera, Italy. PhD Thesis.
- 713
- 714 Cabaniss, H.E., Gregg, P. M., and Grosfils, E.B., 2018. The role of tectonic stress in triggering large  
715 silicic caldera eruptions. Geophysical Research Letters, 45, 3889–3895. [https://doi.org/10.1029/](https://doi.org/10.1029/2018GL077393)  
716 [2018GL077393](https://doi.org/10.1029/2018GL077393) .
- 717
- 718 Cayol, V., and Cornet, F. H., 1998. Effects of topography on the interpretation of the deformation field  
719 of prominent volcanoes: Application to Etna. Geophysical Research Letters, 25(11), 1979–1982.  
720 <https://doi.org/10.1029/98GL51512>.
- 721
- 722 Cailleau, B., T.R. Walter, P. Janle, and E. Hauber, 2003. Modeling volcanic deformation in a regional  
723 stress field: Implications for the formation of graben structures on Alba Patera, Mars, J. Geophys.  
724 Res., 108(E12), 5141, doi:10.1029/2003JE002135.
- 725
- 726 Cailleau B., Thomas R. Walter, Peter Janle, Ernst Hauber, 2005. Unveiling the origin of radial grabens  
727 on Alba Patera volcano by finite element modelling Icarus 176, 44–56.
- 728
- 729 Cabrera-Gutiérrez, R., and Espíndola, J.M., 2010. The 1998-1999 eruption of Volcán de Colima,  
730 Mexico: an application of Maeda's viscoelastic model. Geofísica internacional, 49(2), 83-96.
- 731
- 732 Canales, J.P., Nedimović, M.R., Kent, G.M., Carbotte, S.M., and Detrick, R.S., 2009. Seismic  
733 reflection images of a near-axis melt sill within the lower crust at the Juan de Fuca ridge. Nature,  
734 460(7251), 89.
- 735
- 736 Capra, L., and Macías, J.L., 2002. The cohesive Naranjo debris-flow deposit (10 km<sup>3</sup>): A dam breakout  
737 flow derived from the Pleistocene debris-avalanche deposit of Nevado de Colima Volcano (México).  
738 Journal of Volcanology and Geothermal Research, 117(1-2), 213-235.
- 739
- 740 Capra L, Macías JL, Cortés A, Dávila N, Saucedo R, Osorio-Ocampo S, Arce JL, Galvilanes-Ruiz JC,  
741 Corona-Càvez P, Gàrcia-Sancez L, Sosa-Ceballos G, Vasquez R., 2016. Preliminary report on the July  
742 10–11, 2015 eruption at Volcán de Colima: Pyroclastic density currents with exceptional runouts and

739 volume, *J Volcanol Geotherm Res* 310: 39-49.  
740  
741 Cianetti, S., Giunchi, C., and Casarotti, E., 2012. Volcanic deformation and flank instability due to  
742 magmatic sources and frictional rheology: the case of Mount Etna. *Geophysical Journal International*,  
743 191(3), 939-953.  
744  
745 Charco, M., and Galán del Sastre, P., 2014. Efficient inversion of three-dimensional finite element  
746 models of volcano deformation. *Geophysical Journal International*, 196(3), 1441-1454.  
747  
748 Chaput, M., Pinel, V., Famin, V., Michon, L., and Froger, J.L., 2014. Cointrusive shear displacement  
749 by sill intrusion in a detachment: A numerical approach. *Geophysical Research Letters*, 41(6), 1937-  
750 1943.  
751  
752 Cortés, A., 2005. Carta geológica del complejo volcánico de Colima. UNAM, Instituto de Geología.  
753  
754 Cortés, A., Garduño, V.H., Macías, J. L., Navarro-Ochoa, C., Komorowski, J.C., Saucedo, R., and  
755 Gavilanes, J. C. (2010). Geologic mapping of the Colima volcanic complex (Mexico) and implications  
756 for hazard assessment. *Geol Soc Am Spec Pap*, 464, 249-264.  
757  
758 Cortés, A., Komorowski, J. C., Macías, J. L., Capra, L., and Layer, P. W., 2019. Late Pleistocene-  
759 Holocene debris avalanche deposits from Volcán de Colima, Mexico. In *Volcán de Colima* (pp. 55-  
760 79). Springer, Berlin, Heidelberg.  
761  
762 Costa, A., Sparks, R.S.J., Macedonio, G., and Melnik, O., 2009. Effects of wall-rock elasticity on  
763 magma flow in dykes during explosive eruptions. *Earth and Planetary Science Letters*, 288(3-4), 455-  
764 462.  
765  
766 Costa, A., Gottsmann, J., Melnik, O., and Sparks, R. S. J., 2011. A stress-controlled mechanism for the  
767 intensity of very large magnitude explosive eruptions. *Earth and Planetary Science Letters*, 310(1-2),  
768 161-166.  
769  
770 Currenti, G., Bonaccorso, A., Del Negro, C., Scandura, D., and Boschi, E., 2010. Elasto-plastic  
771 modeling of volcano ground deformation. *Earth and Planetary Science Letters*, 296(3-4), 311-318.  
772  
773 Currenti, G., and Williams, C.A., 2014. Numerical modeling of deformation and stress fields around a  
774 magma chamber: Constraints on failure conditions and rheology. *Physics of the Earth and Planetary*  
775 *Interiors*, 226, 14-27.  
776  
777 Dávila, N., Capra, L., Ferrés, D., Gavilanes-Ruiz, J. C., and Flores, P., 2019. Chronology of the 2014–  
778 2016 Eruptive Phase of Volcán de Colima and Volume Estimation of Associated Lava Flows and  
779 Pyroclastic Flows Based on Optical Multi-Sensors. *Remote Sensing*, 11(10), 1167.  
780  
781 Del Potro, R. and Hürlimann, M., 2008. Geotechnical classification and characterization of materials  
782 for stability analyses of large volcanic slopes. *Eng. Geol.* 98(1), 1–17.  
783  
784 Dieterich J.H., and R.W. Decker, 1975. Finite element modeling of surface deformation associated  
with volcanism, *J. Geophys. Res.*, 80, 4094–4102.  
785  
786 Escudero, C.R., and Bandy, W.L., 2017: Ambient seismic noise tomography of the Colima Volcano  
Complex. *Bull. Volcanol.* 79, 13.

- 787 Fernández, J., Tiampo, K. F., Jentzsch, G., Charco, M., and Rundle, J.B., 2001. Inflation or deflation?  
788 New results for Mayon Volcano applying elastic-gravitational modeling. *Geophysical Research Letters*,  
789 28(12), 2349-2352.  
790
- 791 Ferrari, L., Rosas-Elguera, J., Márquez, A., Oyarzun, R., Doblás, M., and Verma, S.P., 1999. Alkalic  
792 (ocean-island basalt type) and calc-alkalic volcanism in the Mexican volcanic belt: A case for plume-  
793 related magmatism and propagating rifting at an active margin?: Comment and Reply. *Geology*, 27(11),  
794 1055-1056.  
795
- 796 Folch, A., Fernández, J., Rundle, J.B., Martí, J., 2000. Ground deformation in a viscoelastic medium  
797 composed of a layer overlying a half-space: a comparison between point and extended sources.  
798 *Geophys. J. Int.* 140 (1), 37–50.
- 799 Frey, H.M., Lange, R.A., Hall, C.M., Delgado-Granados, H., Carmichael, I.S.E., 2007. A Pliocene  
800 ignimbrite flare-up along the Tepic-Zacoalco rift: evidence for the initial stages of rifting between the  
801 Jalisco block (Mexico) and North America. *Geol. Soc. Am. Bull.* 119, 49–64.  
802 <http://dx.doi.org/10.1130/B25950.1>.
- 803 Fujita, E., Kozono, T., Ueda, H., Kohno, Y., Yoshioka, S., Toda, N., and Ida, Y., 2013. Stress field  
804 change around the Mount Fuji volcano magma system caused by the Tohoku megathrust earthquake,  
805 Japan. *Bulletin of volcanology*, 75(1), 679.  
806
- 807 Gabrieli, A., Wilson, L., and Lane, S., 2015. Volcano–tectonic interactions as triggers of volcanic  
808 eruptions. *Proceedings of the Geologists' Association*, 126(6), 675-682.  
809
- 810 Garduño-Monroy, V.H., Saucedo-Girón, R., Jiménez, Z., Gavilanes-Ruiz, J.C., Cortés-Cortés, A.,  
811 Uribe-Cifuentes, R.M. 1998: La Falla Tamazula, límite suroriental del Bloque Jalisco, y sus relaciones  
812 con el Complejo Volcánico de Colima, México. *Revista Mexicana de Ciencias Geológicas* 15(2), 132–  
813 144.
- 814 Gelman, S.E., Deering, C.D., Gutierrez, F.J., and Bachmann, O., 2013. Evolution of the Taupo  
815 Volcanic Center, New Zealand: petrological and thermal constraints from the Omega dacite.  
816 *Contributions to Mineralogy and Petrology*, 166(5), 1355-1374.  
817
- 818 Geyer, A., and Martí, J., 2009. Stress fields controlling the formation of nested and overlapping  
819 calderas: implications for the understanding of caldera unrest. *Journal of Volcanology and Geothermal*  
820 *Research*, 181(3-4), 185-195.  
821
- 822 Geyer, A., and Gottsmann, J., 2010. The influence of mechanical stiffness on caldera deformation and  
823 implications for the 1971–1984 Rabaul uplift (Papua New Guinea). *Tectonophysics*, 483(3-4), 399-  
824 412.  
825
- 826 Geyer, A., Martí, J., and Villaseñor, A., 2016. First-order estimate of the Canary Islands plate-scale  
827 stress field: Implications for volcanic hazard assessment. *Tectonophysics*, 679, 125-139.  
828
- 829 Gerbault, M., Cappa, F., Hassani, R., 2012. Elasto-plastic and hydromechanical models of failure  
830 around an infinitely long magma chamber. *Geochem. Geophys. Geosyst.* 13, Q03009.  
831 <http://dx.doi.org/10.1029/2011GC003917>.
- 832 Gerbault, M., Hassani, R., Lizama CN, Souche, A., 2018. Three-Dimensional Failure Patterns Around  
833 an Inflating Magmatic Chamber. *Geochemistry, Geophysics, Geosystems*, AGU and the Geochemical  
834 Society, In press.

- 835 Geshi, N., Kusumoto, S., and Gudmundsson, A., 2012. Effects of mechanical layering of host rocks  
836 on dike growth and arrest. *Journal of Volcanology and Geothermal Research*, 223, 74-82.  
837
- 838 Grosfils, E.B., 2007. Magma reservoir failure on the terres- trial planets: Assessing the importance of  
839 gravitational loading in simple elastic models, *J. Volcanol. Geotherm. Res.*, 166, 47–75,  
840 doi:10.1016/j.jvolgeores.2007.06.007.
- 841 Grosfils, E.B., McGovern, P. J., Gregg, P.M., Galgana, G.A., Hurwitz, D.M., Long, S.M., Chestler,  
842 S.R., 2015. Elastic models of magma reservoir mechanics: a key tool for investigating planetary  
843 volcanism. *Geol. Soc. London, Spec. Pub.*, 401(1), 239-267.
- 844 Gudmundsson, A., and Brenner, S.L., 2004. How mechanical layering affects local stresses, unrests,  
845 and eruptions of volcanoes. *Geophysical Research Letters*, 31(16).  
846
- 847 Gudmundsson, A., 2006. How local stresses control magma-chamber ruptures, dyke injections, and  
848 eruptions in composite volcanoes, *Earth-Sci.Rev.*, 79(1–2), 1–31.
- 849 Gudmundsson, A., 2011. *Rock fractures in geological processes*. Cambridge University Press.  
850
- 851 Gudmundsson, A., 2012. Strengths and strain energies of volcanic edifices: implications for  
852 eruptions, collapse calderas, and landslides. *Natural Hazards and Earth System Sciences*, 12(7),  
853 2241.  
854
- 855 Goennermann and Taisne, 2015. *Magma Transport in Dikes*. The Encyclopedia of Volcanoes.  
856 <http://dx.doi.org/10.1016/B978-0-12-385938-9.00010-9>.
- 857 Gottsmann, J., Folch, A., and Rymer, H., 2006. Unrest at Campi Flegrei: A contribution to the  
858 magmatic versus hydrothermal debate from inverse and finite element modeling. *Journal of*  
859 *Geophysical Research: Solid Earth*, 111(B7).  
860
- 861 Gutiérrez, F., and Parada, M.A., 2010. Numerical modeling of time-dependent fluid dynamics and  
862 differentiation of a shallow basaltic magma chamber. *Journal of Petrology*, 51(3), 731-762.  
863
- 864 Hautmann, S., Gottsmann, J., Sparks, R.S.J., Costa, A., Melnik, O., and Voight, B., 2009. Modelling  
865 ground deformation caused by oscillating overpressure in a dyke conduit at Soufrière Hills Volcano,  
866 Montserrat. *Tectonophysics*, 471(1-2), 87-95.
- 867 Heap, M. J., Villeneuve, M., Albino, F., Farquharson, J. I., Brothelande, E., Amelung, F., and Baud,  
868 P., 2020. Towards more realistic values of elastic moduli for volcano modelling. *Journal of*  
869 *Volcanology and Geothermal Research*, 390, 106684.  
870
- 871 Hickey, J., Gottsmann, J., and Mothes, P., 2015. Estimating volcanic deformation source  
872 parameters with a finite element inversion: The 2001–2002 unrest at Cotopaxi volcano, Ecuador, J.  
873 *Geophys. Res. Solid Earth*, 120, 1473–1486, doi:10.1002/2014JB011731.
- 874 Hoek, E. and Brown, E.T, 1997. Practical estimates or rock mass strength. *Int. J. Rock Mech. Min. Sci.*  
875 34, 1165–1186.
- 876 Holohan, E.P., Schöpfer, M. P. J., and Walsh, J.J., 2015. Stress evolution during caldera collapse.  
877 *Earth and Planetary Science Letters*, 421, 139-151.

878 Huang, X., and Zhang, Z., 2012. Stress arch bunch and its formation mechanism in blocky stratified  
879 rock masses. *Journal of Rock Mechanics and Geotechnical Engineering*, 4(1), 19-27.  
880

881 Karlstrom, L., Dufek, J., Manga, M., 2010. Magma chamber stability in arc and continental crust. *J.*  
882 *Volcanol. Geotherm. Res.* 190, 249–270.  
883

884 Kinvig, H. S., Geyer, A., and Gottsmann, J., 2009. On the effect of crustal layering on ring-fault  
885 initiation and the formation of collapse calderas. *Journal of Volcanology and Geothermal Research*,  
886 186(3-4), 293-304.  
887

888 Jaeger, J.C., Cook, N.G., and Zimmerman, R., 2009. *Fundamentals of rock mechanics*. John Wiley and  
889 Sons.  
890

891 Jeanne, P., Guglielmi, Y., Rutqvist, J., Nussbaum, C., and Birkholzer, J., 2017. Field characterization  
892 of elastic properties across a fault zone reactivated by fluid injection. *Journal of Geophysical Research:*  
893 *Solid Earth*, 122(8), 6583-6598.  
894

895 Jellinek, A.M. and DePaolo, D.J., 2003. A model for the origin of large silicic magma chambers:  
896 precursors of caldera-forming eruptions. *Bull. Volcanol.* 65, 363–381.  
897

898 Lister, J.R. and Kerr, R.C., 1991. Fluid-mechanical models of crack propagation and their application  
899 to magma transport in dykes. *Journal of Geophysical Research* 96,10,049–10,077.

900 Long, S.M., and Grosfils, E.B., 2009. Modeling the effect of layered volcanic material on magma  
901 reservoir failure and associated deformation, with application to Long Valley caldera, California.  
902 *Journal of Volcanology and Geothermal Research*, 186(3-4), 349-360.  
903

904 López-Loera, H., Urrutia-Fucugauchi, J., Alva-Valdivia, L., 2011. Estudio aeromagnético del complejo  
905 volcánico de Colima, occidente de México – implicaciones tectónicas y estructurales. *Revista*  
906 *Mexicana de Ciencias Geológicas* 28, 349–370.

907 Lungarini, L., Troise, C., Meo, M., and De Natale, G., 2005. Finite element modelling of topographic  
908 effects on elastic ground deformation at Mt. Etna. *Journal of volcanology and geothermal research*,  
909 144(1-4), 257-271.

910 Luhr, J.F., and Carmichael, I.S., 1985. Contemporaneous eruptions of calc-alkaline and alkaline  
911 magmas along the volcanic front of the Mexican Volcanic Belt. *Geofísica Internacional*, 24(1).  
912

913 Luhr, J.F., and Prestegard, K.L., 1988. Caldera formation at Volcán Colima, Mexico, by a large  
914 holocene volcanic debris avalanche. *Journal of Volcanology and Geothermal Research*, 35(4), 335-348.  
915

916 Luhr JF., 2002. Petrology and geochemistry of the 1991 and 1998-1999 lava flows from Volcan Colima,  
917 Mexico. *J Volcanol Geotherm Res* 117: 169–194.  
918

919 Maccaferri, F., Bonafede, M., and Rivalta, E., 2010. A numerical model of dyke propagation in layered  
920 elastic media. *Geophysical Journal International*, 180(3), 1107-1123.  
921

922 Maccaferri, F., Bonafede, M., and Rivalta, E., 2011. A quantitative study of the mechanisms  
923 governing dike propagation, dike arrest and sill formation. *Journal of Volcanology and Geothermal*  
924 *Research*, 208(1-2), 39-50.  
925

- 926 Maccaferri, F., Rivalta, E., Keir, D., and Acocella, V., 2014. Off-rift volcanism in rift zones  
927 determined by crustal unloading. *Nature Geoscience*, 7(4), 297-300.
- 928
- 929 Maccaferri, F., Smittarello, D., Pinel, V., and Cayol, V., 2019. On the propagation path of magma-  
930 filled dikes and hydrofractures: The competition between external stress, internal pressure, and crack  
931 length. *Geochemistry, Geophysics, Geosystems*, 20(4), 2064-2081.
- 932
- 933 Macías, J.L., Saucedo, R., Gavilanes, J.C., Varley, N., Velasco, García S., Bursik, M.I., Vargas,  
934 Gutiérrez V., Cortés, A., 2006. Flujos piroclásticos asociados a la activi- dad explosiva del Volcán de  
935 Colima y perspectivas futuras. *GEOS* 25(3), 340–351.
- 936 Macías J, Arce J, Sosa G, Gardner JE, Saucedo R., 2017. Storage conditions and magma processes  
937 triggering the 1818CE Plinian eruption of Volcán de Colima. *J Volcanol GeothermRes*  
938 doi:10.1016/j.jvolgeores.2017.02.025.
- 939 Macdonald, K.C., 1982. Mid-ocean ridges: fine scale tectonic, volcanic and hydrothermal pro-  
940 cesses within the plate boundary zone. *Annual Review of Earth and Planetary Sciences* 10, 155–190.
- 941 MacLeod, C.J., Yaouancq, G., 2000. A fossil melt lens in the Oman ophiolite: implications for magma  
942 chamber processes at fast spreading ridges. *Earth and Planetary Science Letters* 176, 357–373.
- 943 Manconi A., Walter TR, and Amelung, F., 2007. Effects of mechanical layering on volcano  
944 deformation. *Geophys. J. Int.* (2007) 170, 952–958.
- 945 Manconi, A., Longpré, M.A., Walter, T.R., Troll, V.R., Hansteen, T.H., 2009. The effects of flank  
946 collapses on volcano plumbing systems. *Geology* 37 (12), 1099–1102.
- 947 Marinou, P. and Hoek, E., 2000. GSI: a geologically friendly tool for rock mass strength estimation.  
948 In: *Proc. GeoEng2000 Conference*, Melbourne, 1422–1442.
- 949 Martí, J., and Geyer, A., 2009. Central vs flank eruptions at Teide–Pico Viejo twin stratovolcanoes  
950 (Tenerife, Canary Islands). *Journal of Volcanology and Geothermal Research*, 181(1-2), 47-60.
- 951
- 952 Massaro S, Sulpizio R, Costa A, Capra L., Lucchi F., 2018. Understanding eruptive style variations at  
953 calc-alkaline volcanoes: the 1913 eruption of Fuego de Colima volcano (Mexico). *Bulletin of*  
954 *Volcanology*, 80:62.
- 955 Massaro, S., Costa, A., Sulpizio, R., Coppola, D., Capra, L., 2019. Cyclic activity of Fuego de Colima  
956 volcano (Mexico): insights from satellite thermal data and non-linear models. *Solid Earth*, 1429-1450.
- 957 Margottini, C., Canuti, P., Sassa, K., 2013. *Landslide science and practice (Vol. 1)*. Berlin: Springer.
- 958
- 959 Masterlark, T., Feigl, K.L., Haney, M., Stone, J., Thurber, C., and Ronchin, E., 2012. Nonlinear  
960 estimation of geometric parameters in FEMs of volcano deformation: Integrating tomography models  
961 and geodetic data for Okmok volcano, Alaska. *Journal of Geophysical Research: Solid Earth*,  
962 117(B2).
- 963
- 964 Medina-Martínez, F., Espíndola, J.M., De la Fuente, M., Mena, M., 1996. A gravity model of the  
965 Colima, México region. *Geofis. Int.* 35(4), 409–414.
- 966 Michaeli, W., 1991. *Extrusionswerkzeuge für Kunststoffe und Kautschuk: Bauarten, Gestaltung und*  
967 *Berechnungsmöglichkeiten*. Hanser Verlag.

968  
969 Moeck, I., Schandelmeier, H. and Holl, H.G., 2009. The stress regime in a Rotliegend reservoir of  
970 the Northeast German Basin. *Int. J. Earth. Sci.* 98, 1643-1654.

971 Mutter, J.C., Carbotte, S.M., Su, W.S., Xu, L.Q., Buhl, P., Detrick, R.S., Kent, G.M., Orcutt, J.A.,  
972 Harding, A.J., 1995. Seismic images of active magma systems beneath the East Pacific Rise between  
973 17-degrees-05's and 17-degrees-35's. *Science* 268, 391–395.

974 Newman, A. V., Dixon, T. H., Ofoegbu, G. I., and Dixon, J. E., 2001. Geodetic and seismic constraints  
975 on recent activity at Long Valley Caldera, California: evidence for viscoelastic rheology. *Journal of*  
976 *Volcanology and Geothermal Research*, 105(3), 183-206.

977  
978 Norini, G., Agliardi, F., Crosta, G., Groppelli, G., and Zuluaga, M.C., 2019. Structure of the Colima  
979 Volcanic Complex: Origin and Behaviour of Active Fault Systems in the Edifice. In *Volcán de Colima*  
980 (pp. 27-54). Springer, Berlin, Heidelberg.

981  
982 Norini G, Capra L, Groppelli G, Agliardi F, Pola A, Cortes A., 2010. Structural architecture of the  
983 Colima Volcanic Complex. *J Geophys Res* 115, B12209.

984  
985 Núñez-Cornú F, Nava FA, De la Cruz-Reyna S, Jiménez Z, Valencia C, García-Arthur R., 1994.  
986 Seismic activity related to the 1991 eruption of Colima Volcano, Mexico. *Bull Volcanol* 56: 228–237.  
987

988 Parfitt, E. A., and L. Wilson, 2008. "The role of volatiles." *Fundamentals of Physical Volcanology*,  
989 64-76.

990  
991 Pinel, V., and Jaupart, C., 2004. Magma storage and horizontal dyke injection beneath a volcanic  
992 edifice. *Earth and Planetary Science Letters*, 221(1-4), 245-262.

993  
994 Pinel, V., Carrara, A., Maccaferri, F., Rivalta, E., and Corbi, F., 2017. A two-step model for dynamical  
995 dike propagation in two dimensions: Application to the July 2001 Etna eruption. *Journal of*  
996 *Geophysical Research: Solid Earth*, 122(2), 1107-1125.

997  
998 Pritchard, M. E., and Simons, M., 2004. An InSAR-based survey of volcanic deformation in the central  
999 Andes. *Geochemistry, Geophysics, Geosystems*, 5(2).

1000  
1001 Rao SS., 1989. *The Finite Element Method in Engineering* second edition. PERGAMON PRESS 1989  
1002 ISBN 0-08-033419-9.

1003 Rao, S.S., 2013. *The Finite Element Method in Engineering: Pergamon International Library of*  
1004 *Science, Technology, Engineering and Social Studies*. Elsevier.

1005  
1006 Reubi, O., Blundy, J., and Varley, N.R., 2013. Volatiles contents, degassing and crystallisation of  
1007 intermediate magmas at Volcan de Colima, Mexico, inferred from melt inclusions. *Contributions to*  
1008 *Mineralogy and Petrology*, 165(6), 1087-1106.

1009  
1010 Reubi, O., Blundy, J., and Pickles, J., 2019. Petrological monitoring of Volcán de Colima magmatic  
1011 system: the 1998 to 2011 activity. In *Volcán de Colima* (pp. 219-240). Springer, Berlin, Heidelberg.  
1012 Rivalta et al., 2019. Stress inversions to forecast magma pathways and eruptive vent location *Sci. Adv.*  
1013 2019; 5:eaau9784 .

- 1014 Rivalta, E., Corbi, F., Passarelli, L., Acocella, V., Davis, T., and Di Vito, M.A., 2019. Stress inversions  
1015 to forecast magma pathways and eruptive vent location. *Science advances*, 5(7), eaau9784.  
1016
- 1017 Robin, C., Mossand, P., Camus, G., Cantagrel, J. M., Gourgaud, A., and Vincent, P.M., 1987. Eruptive  
1018 history of the Colima volcanic complex (Mexico). *Journal of Volcanology and Geothermal Research*,  
1019 31(1-2), 99-113.  
1020
- 1021 Ronchin, E., Masterlark, T., Molist, J. M., Saunders, S., and Tao, W., 2013. Solid modeling techniques  
1022 to build 3D finite element models of volcanic systems: an example from the Rabaul Caldera system,  
1023 Papua New Guinea. *Computers & Geosciences*, 52, 325-333.  
1024
- 1025 Ronchin, E., Geyer, A., and Martí, J., 2015. Evaluating topographic effects on ground deformation:  
1026 insights from finite element modeling. *Surveys in Geophysics*, 36(4), 513-548.  
1027
- 1028 Rosas-Elguera, J., Ferrari, L., Garduño-Monroy, V.H., Urrutia-Fucugauchi, J., 1996: Continental  
1029 boundaries of the Jalisco block and their influence in the Pliocene-Quaternary kinematics of western  
1030 Mexico. *Geology* 24, 921–924.
- 1031 Rosas-Elguera J, Ferrari L, Martinez ML, Urrutia-Fucugauchi J., 1997. Stratigraphy and tectonics of  
1032 the Guadalajara region and triple- junction area, western Mexico. *Int Geol Rev* 39:125–140.  
1033 doi:10.1080/00206819709465263.
- 1034 Rosas-Elguera, J., Alva-Valdivia, L. M., Goguitchaichvili, A., Urrutia-Fucugauchi, J., Ortega-Rivera,  
1035 M. A., Prieto, J.C.S., and Lee, J.K., 2003. Counterclockwise rotation of the Michoacan Block:  
1036 implications for the tectonics of western Mexico. *International Geology Review*, 45(9), 814-826.  
1037
- 1038 Roverato, M., Capra, L., Sulpizio, R., Norini, G., 2011. Stratigraphic reconstruction of two debris  
1039 avalanche deposits at Colima Volcano (Mexico): insights into pre-failure conditions and climate  
1040 influence. *Journal of Volcanology and Geothermal Research*, 207(1-2), 33-46, 2011
- 1041 Roverato, M., and Capra, L., 2013. Características microtexturales como indicadores del transporte y  
1042 emplazamiento de dos depósitos de avalancha de escombros del Volcán de Colima (México). *Revista  
1043 mexicana de ciencias geológicas*, 30(3), 512-525.  
1044
- 1045 Salzer J.T., Nikkhoo M., Walter T., Sudhaus H., Reyes-Dávila G., Bretòn-Gonzalez M., Aràmbula R.,  
1046 2014. Satellite radar data reveal short-term pre-explosive displacements and a complex conduit system  
1047 at Volcan de Colima, Mexico. *Front Earth Sci* 2:12.  
1048
- 1049 Saada, A.S., 2009. *Elasticity: Theory and Applications*. Krieger, Malabar, Florida.
- 1050 Savin, G. N., 1961. Stress concentration around holes.  
1051
- 1052 Saucedo R, Macías J., Gavilanes JC, Arce JL, Komorowski JC, Gardner JE, Valdez-Moreno G., 2010.  
1053 Eyewitness, stratigraphy, chemistry, and eruptive dynamics of the 1913 Plinian eruption of Volcán  
1054 de Colima. México. *J Volcanol Geotherm Res* 191:149–166.  
1055
- 1056 Saucedo R, Macías JL, Gavilanes JC, Arce JL, Komorowski JC, Gardner JE, and Valdez-Moreno G.,  
1057 2011. Corrigendum to Eyewitness, stratigraphy, chemistry, and eruptive dynamics of the 1913 plinian  
1058 eruption of Volcan de Colima, Mexico. *J Volcanol Geotherm Res* 191:149–166.  
1059



- 1060 Schwarz, H.R., 1991. Methode der finiten Elemente neubearbeitete Auflage, B.G. Teubner Stuttgart  
1061 ISBN 3-519-22349-X.
- 1062 Selvans, M. M., Stock, J. M., DeMets, C., Sanchez, O., and Marquez-Azua, B., 2011. Constraints on  
1063 Jalisco Block motion and tectonics of the Guadalajara triple junction from 1998–2001 Campaign GPS  
1064 Data. *Pure and applied geophysics*, 168(8-9), 1435-1447.
- 1065  
1066 Serpa, L., Smith, S., Katz, C., Skidmore, C., Sloan, R., Pavlis, T., 1992. A geophysical investigation  
1067 of the southern Jalisco block in the state of Colima, Mexico. *Geofisica Internacional* 31, 247–252.
- 1068 Simms MA., and Graven G., 2004. Thermal convection in faulted extensional sedimentary basins:  
1069 theoretical results from finite-element modelling. *Geofluids* (2004), 4, 109-130.
- 1070  
1071 Singh, S. C., Crawford, W. C., Carton, H., Seher, T., Combier, V., Cannat, M., and Miranda, J. M.,  
1072 2006. Discovery of a magma chamber and faults beneath a Mid-Atlantic Ridge hydrothermal field.  
1073 *Nature*, 442(7106), 1029.
- 1074  
1075 Sinton, J.M., and Detrick, R.S., 1992. Mid-ocean ridge magma chambers. *Journal of Geophysical*  
1076 *Research: Solid Earth*, 97(B1), 197-216.
- 1077  
1078 Stock JM and Lee J., 1994. Do microplates in subduction zones leave a geological record? *Tectonics*  
1079 13:1472–1487.
- 1080 Stoopes, G. R., and Sheridan, M.F., 1992. Giant debris avalanches from the Colima Volcanic Complex,  
1081 Mexico: Implications for long-runout landslides (> 100 km) and hazard assessment. *Geology*, 20(4),  
1082 299-302.
- 1083  
1084 Spica, Z., Cruz-Atienza, V.M., Reyes-Alfaro, G., Legrand, D., and Iglesias, A., 2014. Crustal imaging  
1085 of western Michoacán and the Jalisco Block, Mexico, from ambient seismic noise. *Journal of*  
1086 *Volcanology and Geothermal Research*, 289, 193-201.
- 1087  
1088 Spica Z, Perton M, Legrand D., 2017. Anatomy of the Colima volcano magmatic system,  
1089 Mexico, *Earth Planet Sci Lett* 459: 1-13.
- 1090  
1091 Suárez, G., Garcia-Acosta, V., Gaulon, R., 1994. Active crustal deformation in the Jalisco block,  
1092 Mexico: evidence for a great historical earthquake in the 16th century. *Tectonophysics* 234, 117–12.
- 1093 Sulpizio, R., Lucchi, F., Forni, F., Massaro, S., and Tranne, C., 2016. Unravelling the effusive-  
1094 explosive transitions and the construction of a volcanic cone from geological data: The example of  
1095 Monte dei Porri, Salina Island (Italy). *Journal of Volcanology and Geothermal Research*, 327, 1-22.
- 1096  
1097 Sulpizio, R., and Massaro, S., 2017. Influence of stress field changes on eruption initiation and  
1098 dynamics: a review. *Frontiers in Earth Science*, 5, 18.
- 1099  
1100 Tibaldi, A., 2015. Structure of volcano plumbing systems: A review of multi-parametric effects.  
1101 *Journal of Volcanology and Geothermal Research* 298 (2015) 85–135.
- 1102 Touloukian, Y.S., Judd, W.R., Roy, R.F., 1989. *Physical Properties of Rocks and Minerals*, vol. 548.  
1103 Hemisphere, New York.
- 1104 Turcotte, D. L. and Schubert, G., 2002. *Geodynamics*, 2nd edition, Cambridge University Press.
- 1105 Zehner B, Jana H. Börner J.H., Görz I., Spitzer K., 2015. Workflows for generating tetrahedral meshes

- 1106 for finite element simulations on complex geological structures. *Computers and Geosciences*, 79, 105-  
1107 117.
- 1108 Zhao, S., Muller, R. D., Takahashi, Y. and Kaneda, Y., 2004. 3-D finite-element modelling of  
1109 deformation and stress associated with faulting: effect of inhomogeneous crustal structures, *Geophys.*  
1110 *J. Int.*, 157, 629– 644.
- 1111 Zhong, X. Marcin, Dabrowski, Bjørn Jamtveit, 2019. Analytical solution for the stress field in elastic  
1112 half space with a spherical pressurized cavity or inclusion containing eigenstrain. *Geophysical*  
1113 *Journal International* · (submitted).
- 1114 Zobin, V.M., Luhr, J.F., Taran, Y.A., Bretón, M., Cortés,A., De la Cruz-Reyna, S., Domínguez, T.,  
1115 Galindo, I., Gavilanes, J.C., Muñiz, J.J., Navarro, C., Ramírez, J. J., Reyes, G.A., Ursúa, M., Velasco,  
1116 J., Alatorre, E., Santiago, H., 2002. Overview of the 1997–2000 activity of Volcán de Colima, Mexico.  
1117 *J. Volcanol. Geotherm.Res.* 117, 1–19.
- 1118  
1119 Watanabe, T., Masuyama, T., Nagaoka, K., Tahara, T., 2002. Analog experiments on magma-filled  
1120 cracks: competition between external stresses and internal pressure. *Earth Planets Space* 54, 1247–  
1121 1261.
- 1122 Wang, R., Martin, F.L. and Roth, F., 2003. Computation of deformation induced by earthquakes in a  
1123 multi-layered elastic crust-FORTRAN programs EDGRN/EDCMP, *Comput. Geosci.*, 29, 195–207.  
1124
- 1125 Eyewitness, stratigraphy, chemistry, and eruptive dynamics of the 1913 plinian eruption of Volcan de  
1126 Colima, Mexico. *J Volcanol Geotherm Res* 191:149–166.  
1127
- 1128 Schwarz, H.R., 1991. *Methode der finiten Elemente neubearbeitete Auflage*, B.G. Teubner Stuttgart  
1129 ISBN 3-519-22349-X.
- 1130 Selvans, M. M., Stock, J. M., DeMets, C., Sanchez, O., and Marquez-Azua, B., 2011. Constraints on  
1131 Jalisco Block motion and tectonics of the Guadalajara triple junction from 1998–2001 Campaign GPS  
1132 Data. *Pure and applied geophysics*, 168(8-9), 1435-1447.  
1133
- 1134 Serpa, L., Smith, S., Katz, C., Skidmore, C., Sloan, R., Pavlis, T., 1992. A geophysical investigation  
1135 of the southern Jalisco block in the state of Colima, Mexico. *Geofisica Internacional* 31, 247–252.
- 1136 Simms MA., and Graven G., 2004. Thermal convection in faulted extensional sedimentary basins:  
1137 theoretical results from finite-element modelling. *Geofluids* (2004), 4, 109-130.  
1138
- 1139 Singh, S. C., Crawford, W. C., Carton, H., Seher, T., Combier, V., Cannat, M., and Miranda, J. M.,  
1140 2006. Discovery of a magma chamber and faults beneath a Mid-Atlantic Ridge hydrothermal field.  
1141 *Nature*, 442(7106), 1029.  
1142
- 1143 Sinton, J.M., and Detrick, R.S., 1992. Mid-ocean ridge magma chambers. *Journal of Geophysical*  
1144 *Research: Solid Earth*, 97(B1), 197-216.  
1145
- 1146 Stock JM and Lee J., 1994. Do microplates in subduction zones leave a geological record? *Tectonics*  
1147 13:1472–1487.

- 1148 Stoores, G. R., and Sheridan, M.F., 1992. Giant debris avalanches from the Colima Volcanic Complex,  
1149 Mexico: Implications for long-runout landslides (> 100 km) and hazard assessment. *Geology*, 20(4),  
1150 299-302.
- 1151
- 1152 Spica, Z., Cruz-Atienza, V.M., Reyes-Alfaro, G., Legrand, D., and Iglesias, A., 2014. Crustal imaging  
1153 of western Michoacán and the Jalisco Block, Mexico, from ambient seismic noise. *Journal of*  
1154 *Volcanology and Geothermal Research*, 289, 193-201.
- 1155
- 1156 Spica Z, Pertou M, Legrand D., 2017. Anatomy of the Colima volcano magmatic system,  
1157 Mexico, *Earth Planet Sci Lett* 459: 1-13.
- 1158
- 1159 Suárez, G., Garcia-Acosta, V., Gaulon, R., 1994. Active crustal deformation in the Jalisco block,  
1160 Mexico: evidence for a great historical earthquake in the 16th century. *Tectonophysics* 234, 117–12.
- 1161
- 1162 Sulpizio, R., Lucchi, F., Forni, F., Massaro, S., and Tranne, C., 2016. Unravelling the effusive-  
1163 explosive transitions and the construction of a volcanic cone from geological data: The example of  
1164 Monte dei Porri, Salina Island (Italy). *Journal of Volcanology and Geothermal Research*, 327, 1-22.
- 1165
- 1166 Sulpizio, R., and Massaro, S., 2017. Influence of stress field changes on eruption initiation and  
1167 dynamics: a review. *Frontiers in Earth Science*, 5, 18.
- 1168
- 1169 Tibaldi, A., 2015. Structure of volcano plumbing systems: A review of multi-parametric effects.  
*Journal of Volcanology and Geothermal Research* 298 (2015) 85–135.
- 1170
- 1171 Touloukian, Y.S., Judd, W.R., Roy, R.F., 1989. *Physical Properties of Rocks and Minerals*, vol. 548.  
Hemisphere, New York.
- 1172
- 1173 Turcotte, D. L. and Schubert, G., 2002. *Geodynamics*, 2nd edition, Cambridge University Press.
- 1174
- 1175 Zehner B, Jana H. Börner J.H., Görz I., Spitzer K., 2015. Workflows for generating tetrahedral meshes  
for finite element simulations on complex geological structures. *Computers and Geosciences*, 79, 105-  
117.
- 1176
- 1177 Zhao, S., Muller, R. D., Takahashi, Y. and Kaneda, Y., 2004. 3-D finite-element modelling of  
1178 deformation and stress associated with faulting: effect of inhomogeneous crustal structures, *Geophys.*  
*J. Int.*, 157, 629– 644.
- 1179
- 1180 Zhong, X. Marcin, Dabrowski, Bjørn Jamtveit, 2019. Analytical solution for the stress field in elastic  
1181 half space with a spherical pressurized cavity or inclusion containing eigenstrain. *Geophysical*  
*Journal International* · (submitted).
- 1182
- 1183 Zobin, V.M., Luhr, J.F., Taran, Y.A., Bretón, M., Cortés, A., De la Cruz-Reyna, S., Domínguez, T.,  
1184 Galindo, I., Gavilanes, J.C., Muñiz, J.J., Navarro, C., Ramírez, J. J., Reyes, G.A., Ursúa, M., Velasco,  
1185 J., Alatorre, E., Santiago, H., 2002. Overview of the 1997–2000 activity of Volcán de Colima, Mexico.  
*J. Volcanol. Geotherm.Res.* 117, 1–19.
- 1186
- 1187 Watanabe, T., Masuyama, T., Nagaoka, K., Tahara, T., 2002. Analog experiments on magma-filled  
1188 cracks: competition between external stresses and internal pressure. *Earth Planets Space* 54, 1247–  
1189 1261.
- 1190
- 1191 Wang, R., Martin, F.L. and Roth, F., 2003. Computation of deformation induced by earthquakes in a  
1192 multi-layered elastic crust-FORTRAN programs EDGRN/EDCMP, *Comput. Geosci.*, 29, 195–207.

1193  
1194  
1195  
1196  
1197